DELFT UNIVERSITY OF TECHNOLOGY

MASTER THESIS

Towards a Multi-site Kitaev Chain on Semiconducting-Superconducting Hybrid Nanowires

Author: Xiang Li

Student Number: 5278198

Committee: Dr. M. Wimmer (Supervisor)
Dr. F. Sebastiano
Dr. R. Ishihara
Dr. T. Dvir (Daily Supervisor)
A. Bordin (Daily Supervisor)

A thesis submitted in fulfillment of the requirements for the degree of Master of Science in Electrical Engineering.

December 15, 2022

TU Delft

Towards a Multi-site Kitaev Chain on Semiconducting-Superconducting Hybrid Nanowires

XIANG LI

Electrical Enegineering, Mathematics & Computer Science,
Delft University of Technnology

Abstract

A minimal Kitaev chain can be realized by coupling two quantum dots to a superconductor on both sides. Andreev Bound States inside the superconductor mediate two types of interdot couplings: Cross Andreev Reflection (CAR) and Elastic Co-tunneling (ECT). Spin-orbit interaction (SOI) enables equal strengths of CAR and ECT, where Majorana Bound States with a quadratic protection emerge. By extending the chain to more dots, the protection is predicted to become stronger.

In this project, semiconducting-superconducting InSb nanowires provide both SOI and superconductivity. We develop systematic procedures to tune a two-site device to hold Majorana Bound States. Next, quantum transport processes on a three-site device are studied. Sequential processes combining CAR and ECT are observed.

Contents

Introduction

In condensed matter systems, quasiparticles that are equal to their own antiparticles are called Majorana Bound States (MBS) [1, 2]. MBS are neither fermions nor bosons since they are predicted to obey non-abelian statistics [3]. In real systems, MBS must appear in pairs, meaning that a superposition of two MBS forms a single fermionic state. In particular, a pair of spatially separated MBS defines a delocalized fermion, which is protected from local perturbations [2].

In 2001, A. Kitaev proposed that MBS can appear at the ends of a one-dimensional chain [4]. The Kitaev chain is composed of N fermionic sites which can host one electron each. Moreover, spin degeneracy is lifted for each electron. Adjacent sites are coupled by two mechanisms: hopping of one electron from one site to the next, and pairing of two electrons from both sites. It is known that superconductivity can pair electrons of anti-parallel spins [5] (also known as s-wave or singlet pairing). However, if all the sites share the same spin species, superconducting pairing between parallel spins is required. This kind of pairing is referred to as p-wave or triplet pairing. Though a few natural materials are predicted to have this non-trivial superconductivity, such as Sr_2RuO_4 [6], the majority interest of the community is still laying on engineering p-wave superconductivity starting from ordinary superconductors with spin-orbit interaction as an extra ingredient [7, 8].

In the past ten years, the community was concentrating on combining the spin-orbit interaction with the semiconducting nanowires which can be viewed as the continuum limit of the Kitaev chain [9, 10]. With carefully selected parameters, the nanowire can be driven into a topological phase holding Majorana Bound States [11]. However, the detection of Majorana Bound States is controversial in past experiments. Chemical potential disorder along the

nanowire can break the topological phase of the system and might lead to quantum states mimicking MBS [12].

In this project, we follow a new approach presented in chapter 1 that aims to realize a Kitaev chain with an array of quantum dots alternated by short superconducting segments. The effects of the disorder can be greatly suppressed since the chemical potentials on the dots can be individually tuned and hence can compensate for disorder [13]. It has been proposed that a single superconductor coupled with only two quantum dots on each side can implement a minimal Kitaev chain, also referred to as the Poor-Man Majorana model [14].

The Poor-Man Majorana model was realized for the first time in 2021 [15]. The first target of my project is to reproduce the Poor-Man Majorana system again on a newly fabricated device with a systematic procedure (chapter 3). The second target is to extend the Poor-Man Majorana model to a three-site Kitaev chain (chapter 4). During the second stage, nanofabrication techniques presented in chapter 2 are also performed.

Chapter 1

Theory

This chapter presents necessary theories about all the key components used in realizing the multi-site Kitaev Chain, which will be introduced first. In the following sections, important properties of quantum dots and superconductors are introduced. For the semiconductor nanowire, spin-orbit interaction is the core for inducing triplet Cooper pairing. In the end, the Hamiltonian of the two and three-site systems is analyzed, which connects the theory to the measurements in the real device.

1.1 Kitav Chain Theory

Kitaev's paper [4] proposed a toy model, which potentially holds Majorana quasiparticles. The system is modeled by a chain with N fermions with no spin degeneracy, shown in figure 1.1. Fermions can either hop between adjacent sites with rate t or have pairing rate Δ between two sites. The amplitude Δ is referred to as triplet pairing within electrons with the same spin species. Considering the on-site chemical potential μ_i on-site i, the system Hamiltonian can be expressed with creation/annihilation operators for each site.

$$H = -\sum_{i=1}^{N} \mu_i c^\dagger c + \sum_{i=1}^{N-1} -t c_i c_{i+1}^\dagger + \Delta c_i c_{i+1} + h.c. \tag{1.1}$$

By introducing a transformation on the operator c_i for each site

$$c_i, c_i^\dagger = \frac{1}{2}(\gamma_{i,1} \pm i\gamma_{i,2}) \tag{1.2}$$

the Hamiltonian 1.1 can be translated into γ language, where $\gamma_{i,j} = \gamma_{i,j}^\dagger$ is held.

$$H = \frac{i}{2}\sum_{i=1}^{N-1} -\mu\gamma_{i,1}\gamma_{i,2} + (t + \mathrm{Re}\{\Delta\})\gamma_{\mathrm{i},2}\gamma_{\mathrm{i+1},1} + (-\mathrm{t} + \mathrm{Re}\{\Delta\})\gamma_{\mathrm{i},1}\gamma_{\mathrm{i+1},2} \tag{1.3}$$

The interesting point appears when taking the real part of pairing amplitude $\mathrm{Re}\{\Delta\} = \mathrm{t}$ and $\mu_i = 0$. The Hamiltonian is thus only composed of inter-site γ pairs, shown in figure 1.1(b). Furthermore, the unpaired $\gamma_{1,1}$ and $\gamma_{N,2}$ distributed at the two ends of the chain form zero energy Majorana quasiparticles. They together define a delocalized fermion: $c_M = \frac{1}{2}(\gamma_{N,2} + i\gamma_{1,1})$

One might notice that there is no restriction on hopping amplitudes t_i and t_j on different pairs of sites, so a more general condition to have Majoranas on the Kitaev chain derived in [13] is expressed as $t_i = |\Delta_i|$ with all pairing amplitudes $\{\Delta_i\}$ sharing the same phase.

1.2 Fundamentals of Quantum Dots

The spinless Kitaev chain in the previous section can be realized by feeding the N sites with electrons of a single spin species. In our approach, these N sites are implemented with N quantum dots. Quantum dots play an important role to filter electron spins in a magnetic field.

In figure 1.2(a), the quantum dot can be imagined as an island confined with tunnel barriers to drain and source, and the electrochemical potential on the island is tuned by the dot plunger. The equivalent circuits of the dot island in figure 1.2(b) model barriers and plunger gate with capacitances C_s, C_d, and C_g respectively. The $N+1$th electron tunnels in an $N-$electron island should pay a piece of extra energy $E_{add} = \mu_{N+1} - \mu_N$ to overcome Coulomb repulsion [16] and the addition energy can be explicitly expressed as

$$E_{add} = 2E_c + \Delta E \tag{1.4}$$

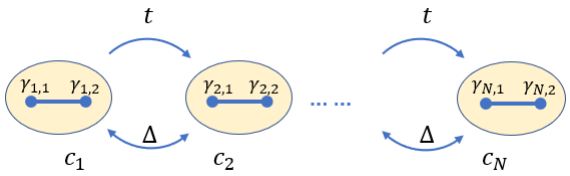

(a)

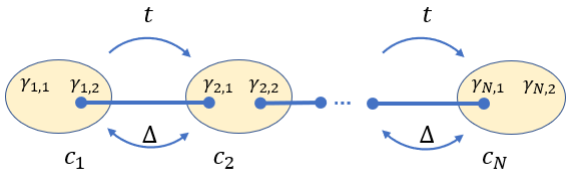

(b)

Figure 1.1: *(a) Trivial phase of Kitaev chain. (b) Non-trivial phase of Kitaev chain.*

where $E_c = \frac{e^2}{2C}$ is defined as charging energy and C is summation $C_g+C_s+C_d$. Especially, when considering the $N+1$th electron occupies a new quantum state of the dot, the energy level splitting between states contributes to the term ΔE in E_{add}.

An important phenomenon given by the charging effect on the island is the Coulomb blockade. When the potential of an electron is not aligned within the window between bias and drain, the current flow will be blockaded. On the contrary, the blockade lifts if aligning happens, leading to a current governed by the tunneling rates Γ_d and Γ_s [17]. By plotting the current on the 2D diagram of $V_{SD} = \mu_D - \mu_S$ against V_{gate}, the region where blockade happens forms a series of Coulomb diamonds. In each diamond, the charge number on the island is fixed. The height of the diamond is limited by addition energy E_{add} and the slope k depends on the ratio between capacitances shown in figure 1.2(c). In addition, the red lines near the diamond border are contributed by excited states. The Coulomb diamond tells useful information about the lever arm between the chemical potential on leads and the plunger gate V_{gate}, as well as relative drain and source couplings.

Noticing that the spins of electrons on μ_{N+1} and μ_N from the same quantum

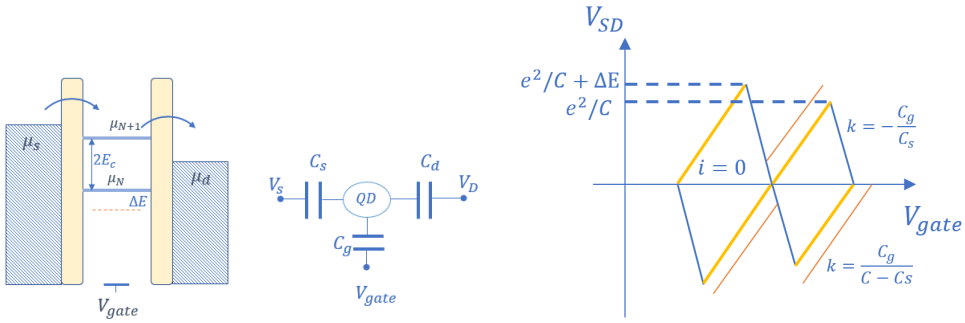

(a) (b) (c)

Figure 1.2: *(a) Dot sketch. (b) Dot equivalent circuit. (c) Coulomb diamond.*

dot state are opposite due to fermionic statistics. When applying an external magnetic field to the dot and assuming the dot material is paramagnetic, μ_N is preferred for the lower energy electron state with spin orientation along the field, while μ_{N+1} has no choice to choose the other. With this property, spins can be filtered.

1.3 Fundamentals of Superconductivity

1.3.1 BCS Theory

Before introducing advanced properties in superconductors, some fundamentals need to be presented first. Bardeen-Cooper-Schrieffer (BCS) theory [5] tells that at $T = 0K$ a pair of electrons is favored for the ground state (bounded Cooper pairs) in superconductor Fermi sea instead of a single electron due to a net attractive interaction between electrons. When the attractive interaction is caused by phonon-electron coupling, the superconductor is normal or $s-$wave type, meaning opposite spins form a Cooper pair. The Hamiltonian can be expressed in terms of electron kinetic energy ϵ_k with momentum $\mathbf{k}$, spin $\sigma = \{\uparrow, \downarrow\}$, pairing amplitude Δ and Fermi energy of superconductor E_F,

$$H_{BCS} = \sum_{|k|>k_F,\sigma} (\epsilon_k - E_F)\hat{n}_{k,\sigma} + \sum_{|k|>k_F} \Delta c^{\dagger}_{k,\uparrow} c^{\dagger}_{-k,\downarrow} + h.c. \tag{1.5}$$

An Bogoliubov-de Gennes format of H_{BCS} is then

$$H_{BCS}^{BdG} = \begin{pmatrix} \epsilon_k - E_F & \Delta \\ \Delta^* & -\epsilon + E_F \end{pmatrix} \tag{1.6}$$

The eigenvalue of 1.6 is $\sqrt{(\epsilon_k - E_F)^2 + \Delta^2}$, which indicates a gap of Δ between the BCS ground state and its excitation. Noticing the basis chosen for H_{BCS}^{BDG} is the Nambu spinor $\Psi^\dagger = (c_{k,\uparrow}^\dagger, c_{-k,\downarrow})$, the eigenstates of 1.6 can be written in a superposition of electron and hole, also known as Bogoliubov quasi-particle.

In addition, when a normal metal or semiconductor is attached to a superconductor, superconductivity could be induced at the normal side at a finite depth and below a certain temperature [18]. This effect is called the proximity effect.

1.3.2 Andreev Reflection

When considering shooting an electron with energy $E < \Delta$ to a Normal-Superconducting (N-S) interface, aside from being reflected by the interface, a sub-gap process, Andreev Reflection (AR), might happen. In AR, a hole is retro-reflected to the N side, meaning that a Cooper pair of electrons is transmitted through the interface to the superconductor Fermi sea. The wave vector of the transmitted electron wave function has an imaginary part [19], indicating an evanescent wave inside the superconductor with depth δ comparable to the superconductor coherent length ξ. Moreover, if considering an N-S-N junction, the hole can also appear on the other side, leading to a non-local transport called Cross Andreev Reflection (CAR).

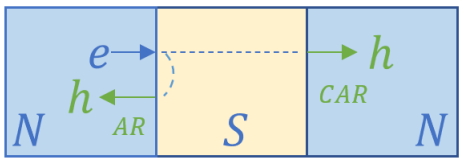

Figure 1.3: *Local Andreev Reflection (AR) and Cross Andreev Reflection (CAR).*

$$\delta = \frac{\hbar v_F}{2\Delta}\sqrt{1-(\frac{E}{\Delta})^2} \approx \xi(T) \tag{1.7}$$

1.3.3 Andreev Bound State

Consider an insulating-normal-superconducting (I-N-S) junction in figure 1.4. The retro-reflected hole of an electron is bounced back by the insulator interface and it can Andreev Reflect again into an electron. When the electron is bounced by the insulator also, an Andreev Reflection cycle is completed. This whole process will lead to a bounded state inside the superconductor gap, known as the Andreev Bound State (ABS). The ABS is considered to be a superposition of electron and hole with components u and v for each.

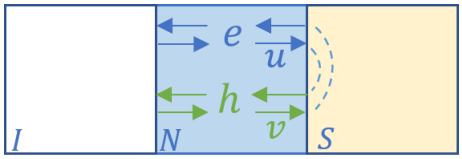

Figure 1.4: *Formation of ABS.*

Furthermore, if the normal metal in figure 1.4 is changed to a quantum dot coupled to the superconductor with coupling Γ_S, the charging energy E_C on this dot should be taken into account, shown in figure 1.5(a). The Anderson Impurity Model describes the Hamiltonian of an ABS on the dot [20]. In Equ 1.8, the basis are chosen to be $\{|0\rangle, |\uparrow\downarrow\rangle, |\downarrow\rangle, |\uparrow\rangle\}$. ϵ_0 represents the dot level and E_z is the Zeeman energy split on the spin if an external magnetic field is switched on. The coupling Γ_S couples $|0\rangle$ with $|\uparrow\downarrow\rangle$ through Andreev Reflection.

$$H = \begin{pmatrix} 0 & \Gamma_S & 0 & 0 \\ \Gamma_S & 2E_C + 2\epsilon_0 & 0 & 0 \\ 0 & 0 & \epsilon_0 - E_z & 0 \\ 0 & 0 & 0 & \epsilon_0 + E_z \end{pmatrix} \tag{1.8}$$

The eigenvalues of the Hamiltonian in Equ 1.9 can be divided into two categories according to the parity of the eigenstates. The odd parity state is a single electron state with a certain spin, also called doublet state $|D\rangle = \{|\uparrow\rangle, |\downarrow\rangle\}$. Meanwhile, the even parity state describes a superconducting-like

superposition, also known as singlet state $|S_-\rangle = u|0\rangle + v|\uparrow\downarrow\rangle$ or $|S_+\rangle = v|0\rangle - u|\uparrow\downarrow\rangle$.

$$\begin{cases} E_{\downarrow,\uparrow} = \epsilon_0 \mp E_z, & \textit{odd parity} \\ E_{S,\pm} = E_C\left[1 + \frac{\epsilon_0}{E_C} \pm \sqrt{(1+\frac{\epsilon_0}{E_C})^2 + (\frac{\Gamma_S}{E_C})^2}\right], & \textit{even parity} \end{cases} \tag{1.9}$$

When $E_z = 0$, the singlet ground state $E = \epsilon_0$ and the doublet ground state $E_{S,-}$ are degenerated on the dome profile shown in figure 1.5(b), which is expressed as

$$\sqrt{(1+\frac{\epsilon_0}{E_C})^2 + (\frac{\Gamma_S}{E_C})^2} = 1 \tag{1.10}$$

On the orange cutting line across the dome in figure 1.5(b), the charging energy on the dot is dominant and the ground state of the dot experience a transition from $|S\rangle \to |D\rangle \to |S\rangle$ while varying ϵ_0. When the cutting line is lifted above the top of the dome, shown as the blue line, the coupling to the superconductor competes over the charging energy and the global ground state always prefers a superconducting-like singlet state.

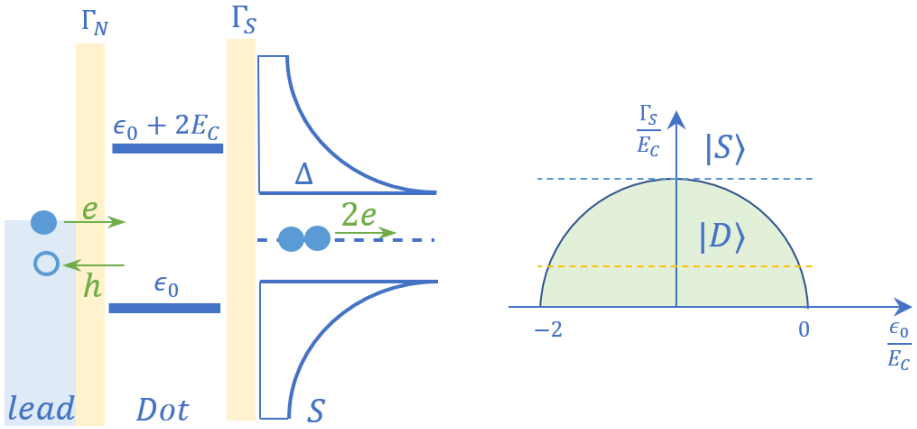

(a) (b)

Figure 1.5: *(a) A dot coupled to a superconductor. The picture is modified from [21]. (b) The ground state is the singlet outside the dome and is the doublet inside the dome.*

1.3.4 Sub-gap Processes Mediated by ABS

Cross Andreev Reflection can be used to pair electrons in the Kitaev model. However, the problem is that the strength of sub-gap non-local transport is attenuated exponentially along the superconductor [22]. To solve this, ABSs residing in the superconducting segment between dots can be considered. The role of ABSs is to mediate interdot coupling as an intermediate state [23]. Figure 1.6(a) and 1.6(b) show this idea in terms of the CAR and Elastic Co-tunneling (ECT) process. The CAR-type interdot coupling and the ECT-type coupling implement Δ and t in the Kitaev chain proposal respectively.

In ABS-mediated transport, an important assumption is that the ABS has a singlet ground state. The superconducting segment mediating interdot couplings in the experiments is a semiconducting nanowire segment with the proximity effect, also called the hybrid dot. A singlet ABS ground state is favored in the hybrid dot due to a large coupling Γ_S to the superconductor shell compared to its charging energy E_C.

Electrons with energy $|E| < E_{ABS}$ virtually charge the ABS by driving it to the doublet excitation state. Then the electron will be relaxed by the ABS either to the opposite side still with energy E or recombined with an electron from the opposite side with energy $-E$ into Cooper pair. These two processes corresponding to ECT and CAR processes are shown in figure 1.6(b) and figure 1.6(a) respectively.

According to [23], at a zero external magnetic field, the ECT and CAR couplings $\Gamma_{\sigma,\eta}^{ECT,CAR}$ between left and right dots with spins σ and η are expressed in Equ 1.11

$$\begin{cases} \Gamma_{\sigma,\eta}^{CAR} = t_L t_R \frac{2uv}{E_{ABS}}(1-\delta_{\sigma,\eta}) \\ \\ \Gamma_{\sigma,\eta}^{ECT} = t_L t_R \frac{u^2-v^2}{E_{ABS}}\delta_{\sigma,\eta} \end{cases} \tag{1.11}$$

where u and v are coefficients of the intermediate ABS state $|S\rangle = u\,|0\rangle + v\,|\uparrow\downarrow\rangle$. t_L and t_R are effective couplings between the left or right dot and the superconductor with the assumption $t_{L,R}$ less than the superconductor gap. $\delta_{i,j}$ is defined as 1 when $i = j$ and 0 when $i \neq j$.

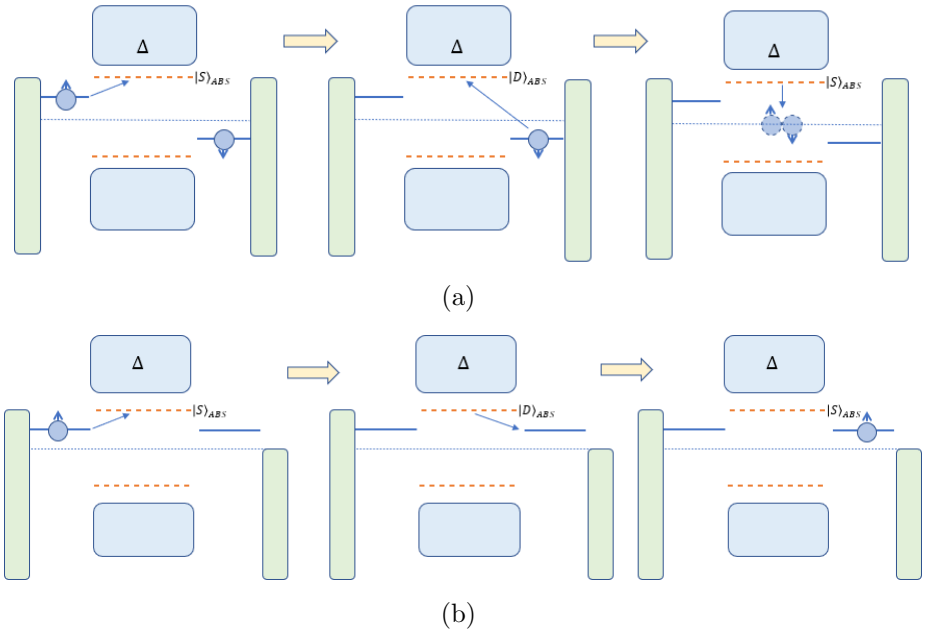

Figure 1.6: *ABS acts as an intermediate state in (a) CAR and (b) ECT.*

1.4 Spin-Orbit Interaction

The spin-orbit interaction universally exists with electrons moving inside a potential V with momentum $\mathbf{p}$, for example, from nuclei. The electron spin interacts with the potential, appearing as a high-order correction to the Dirac equation

$$\Delta H \propto \sigma \cdot (\nabla V \times \mathbf{p}) \tag{1.12}$$

Since inversion symmetry ($\mathbf{r} \to -\mathbf{r}$) and time-reversal symmetry are held in most occasions, Kramer's degeneracy on electron spins is not lifted.

Rashba spin-orbit interaction [24] is a kind of spin-orbit interaction originating from crystal losing inversion symmetry along certain orientation, leading to a certain electric field $\mathbf{E}_R = \nabla V_R$. From the inertial frame of a moving electron, it feels the Rashba electric field as a magnetic field

$$\mathbf{B}_R = \mathbf{v} \times \mathbf{E}_R / c^2 \tag{1.13}$$

In terms of this effective magnetic field, opposite spins of electrons will pre-

cess in different directions around $\mathbf{B}_R$. With this effect, electrons with the same spins can pair into Cooper pairs, creating an effective triplet pairing. When considering the spin-orbit interaction, the expression of CAR interdot coupling between the same spin species $\Gamma^{CAR}_{\uparrow,\uparrow}$ or $\Gamma^{CAR}_{\downarrow,\downarrow}$ will be lifted from zero. When $\Gamma^{CAR}_{\uparrow,\uparrow} = \Gamma^{ECT}_{\uparrow,\uparrow}$ is satisfied, the requirement for observing Majoranas on a two-site Kitaev chain is also met. This special point is called the Majorana Sweet Point in the following chapters.

1.5 Multi-site Kitaev Chain Hamiltonian

1.5.1 BdG Formalism

So far the physics for a practical Kitaev chain is prepared. The BdG Hamiltonian for an N-site Kitaev chain device is expressed with individual on-site potential μ_i, hopping and pairing strength t_i, and Δ_i between each pair.

$$\mathbf{H}^N_{2N\times 2N} = \begin{pmatrix} \mathbf{A}_{N\times N} & \mathbf{B}_{N\times N} \\ \mathbf{B}^\dagger_{N\times N} & -\mathbf{A}_{N\times N} \end{pmatrix} \tag{1.14}$$

where

$$\mathbf{A}_{N\times N} = \begin{pmatrix} \mu_1 & t_1 & 0 & \cdots \\ t_1 & \mu_2 & t_2 & \cdots \\ 0 & t_2 & t_3 & \ddots \\ \vdots & \vdots & \ddots & \ddots \end{pmatrix} \tag{1.15}$$

and

$$\mathbf{B}_{N\times N} = \begin{pmatrix} 0 & \Delta_1 & 0 & \cdots \\ -\Delta_1 & 0 & \Delta_2 & \cdots \\ 0 & -\Delta_2 & 0 & \ddots \\ \vdots & \vdots & \ddots & \ddots \end{pmatrix} \tag{1.16}$$

When $N = 2$, the two site devices will obtain quadratic protection on the zero mode energy [14], which means that the ground state energy $|E| \approx \frac{\mu_1\mu_2}{2\Delta}$ is bounded by the product of the fluctuations on the dot potentials at the vicinity of the sweet point. Nevertheless, the protection will be enhanced greatly if N goes to a large number [13, 25].

1.5.2 Two-site Hamiltonian

For the minimal realization of the two-site device, the Hamiltonian rewrote in the dot number basis $\{|00\rangle, |11\rangle, |01\rangle, |10\rangle\}$ tells about the system directly.

$$H = \begin{pmatrix} 0 & \Delta & 0 & 0 \\ \Delta & \mu_1 + \mu_2 & 0 & 0 \\ 0 & 0 & \mu_1 & t \\ 0 & 0 & t & \mu_2 \end{pmatrix} \tag{1.17}$$

The pairing amplitude Δ only appears in the even parity sub-block of the matrix in Equ 1.17. Meanwhile, the hopping amplitude t governs the odd parity sub-block. Each sub-block has eigenvalues

$$\begin{cases} E_{even} = \frac{\mu_1+\mu_2}{2} \pm \sqrt{(\frac{\mu_1+\mu_2}{2})^2 + \Delta^2} \\ E_{odd} = \frac{\mu_1+\mu_2}{2} \pm \sqrt{(\frac{\mu_1-\mu_2}{2})^2 + t^2} \end{cases} \tag{1.18}$$

In real device measurement, the global ground state is always occupied by either an odd ground state or an even ground state. When switching the parity of the global ground state, the charge flow gives an electronic signal. Therefore, by setting $E_{even,-} = E_{odd,-}$. the parity degeneration condition can be obtained.

$$\mu_1\mu_2 = \Delta^2 - t^2 \tag{1.19}$$

Equ 1.19 indicates a hyperbola profile on the $\mu_1 - \mu_2$ diagram. Moreover, the orientation of the hyperbola directly determines the sign of $|\Delta| - |t|$, and the minimum distance of the two hyperbola branches is given by $d^2_{min} = 8|\Delta^2 - t^2|$. Nevertheless, according to Section 1.2, due to the capacitance lever arm on dot potential μ, a global factor is needed to translate the dot plunger gate voltage into the dot potential.

1.5.3 Three-site situation

When $N = 3$, the phase between two superconductors should be taken into account as a novel degree of freedom. Assuming pure Rashba spin-orbit interaction participates in the transport at zero fields, the relative phase between two superconductors could only be 0 or π [13]. When the relative phase takes π, the first excited state is degenerated with the ground state on the energy spectrum of the Kitaev chain, shown in figure 1.7(b).

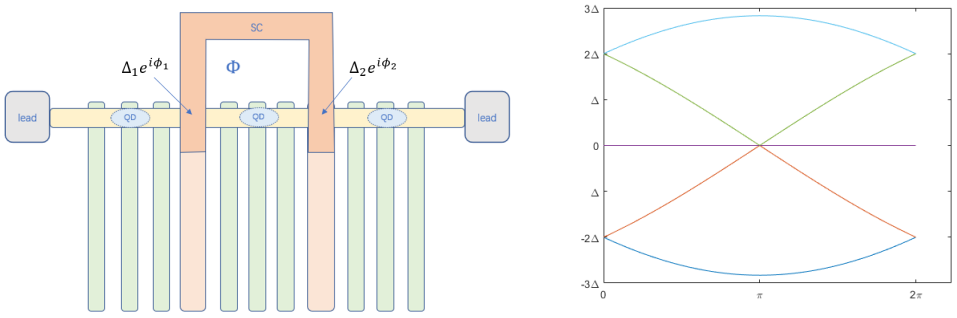

(a) (b)

Figure 1.7: *(a) Two superconductors have individual phase ϕ_1 and ϕ_2. To tune the relative phase, superconductors are fabricated as a loop so that the magnetic flux passing the loop drives the phase shift. (b) The energy spectrum of the Kitaev chain when shifting the relative phase from $0 \to 2\pi$ continuously. Assume $t_1 = t_2 = |\Delta_1| = |\Delta_2|$ in the simulation.*

Chapter 2

Device Fabrication and Measurement Techniques

In the first part of this chapter, all the main techniques involved with device nanofabrication will be presented in a stacked manner. And in the second part, measurement techniques applied to the device will be described, which includes the PCB bonding, dilution refrigerator, and peripheral electronic instructments.

2.1 Nanofabrication Techniques

2.1.1 Kitaev Device Overview

A Kitaev chain is fabricated mainly in seven sequential steps from (a) to (g), shown in figure 2.1. The right and left three gates define two quantum dots capacitively over the dielectric layer (c), while the middle gate is aligned to the superconductor (f) for electric control. Each gate, normal contact, and superconducting contact on the device is routed to a corresponding pad for connecting electronic instruments later. For multi-site devices, one can simply fabricate more alternating dots and superconductors along the horizontal direction without changing the total design significantly. Especially for a three-site device, eleven control gates, two normal contacts, and two superconducting contacts are required.

The detailed techniques applied in the fabrication come into mainly five cate-

gories. Electron Beam Lithography (EBL) is the most fundamental one. It is used to create patterns on the substrate. Physical Vapour Deposition (PVD) can then create metal structures on the substrate. It includes evaporation technique for (a) and (g), and sputtering for (b). The dielectric layer (c) is a metal oxide and it is grown by a chemical process called Atomic Layer Deposition (ALD). The nanowire is grown with the Metal Organic Vapour Phase Epitaxy approach and is deposited manually with a micromanipulator. Last, the superconductor (f) is deposited on the nanowire using the combination of the Smart Wall (SW) technique and evaporation. My contributions to the fabrication process include EBL, HSQ, and metal sputtering.

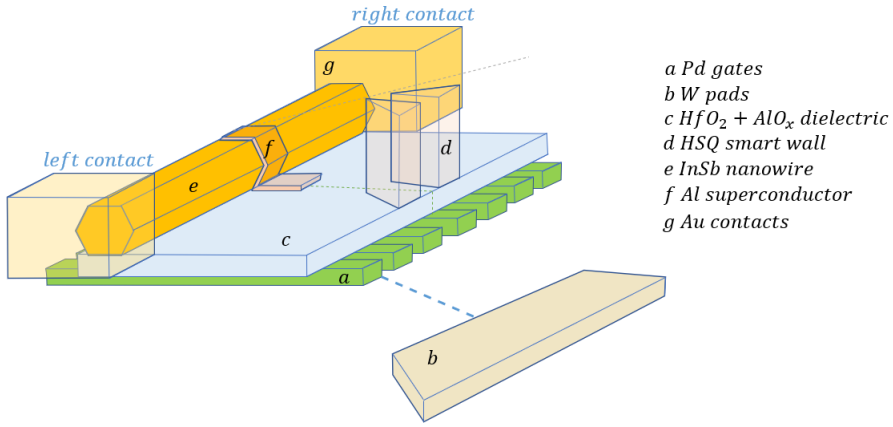

Figure 2.1: *A 3D sketch of the two-site Kitaev device. The chemical element and function for each component are listed from (a) to (g).*

2.1.2 Electron Beam Lithography

Electron Beam Lithography (EBL) [26] is widely used in nanofabrication which enables nanoscale or microscale structures with specific patterns on a substrate. To be strict, the common positive EBL is introduced in this section, while the negative version will be mentioned in a later section. Figure 2.2 shows how EBL plays its role in a metal deposition example.

In the first step (a), EBL resist is coated to the substrate using the technique of spin-coating which spins the substrate with high speed and enables the liquid resist on it spread uniformly. Then in step (b), being exposed to

electron beams focused by a series of lenses, desired patterns could be transferred to the resist. To have a high resolution on the pattern, electron beams are used instead of photons due to their shorter wavelength. After exposure, the exposed region on the resist is ready to be dissolved by a mixture of 4-methyl-pentane-2-one (MIBK) and 2-propanol (IPA), which is the so-called development in (c). After metals are deposited, acetone is used to lift off the rest of the resist, leaving only the desired structure on the substrate as shown in (e).

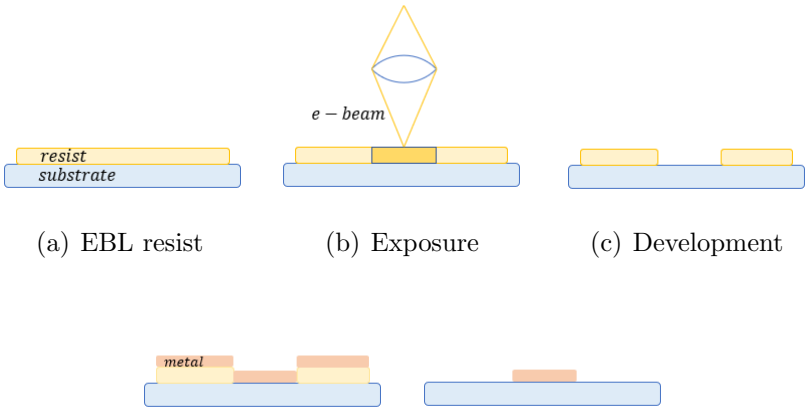

(a) EBL resist (b) Exposure (c) Development

(d) Metal evaporation (e) Lift-off

Figure 2.2: *Workflow for a metal deposition process using EBL.*

2.1.3 Physical Vapour Deposition

Physical Vapour Deposition (PVD) is an important approach to depositing metallic thin films on a substrate. Evaporation and sputtering are two main branches of PVD.

In the Kitaev device, evaporation is applied to fabricate the gates and contacts. A high energy electron beam is shooted to the target metal source. When the metal is melted, the evaporated atoms will fly directly to the substrate in the vacuum chamber. To monitor the deposition rate, a crystal quartz is also receiving the evaporated metal atoms. The tiny weight increasing on the quartz finely changes its resonance frequency, which can be

a perfect sensor of the thickness increment during unit time [27]. In order to have better stickiness to the substrate, the palladium gate and gold contacts are not evaporated directly. Instead, a thin layer of titanium and chromium is padded in the middle respectively. And especially for the contact, since it locates upon the InSb nanowire, an argon milling process is performed before evaporation to physically remove the native oxide on the nanowire.

On the other hand, the pads are sputtered with tungsten. In the sputtering machine, the substrate acts as the anode, and the target metal source acts as the cathode [27]. Argon ions bombard the source and knock off some atoms, which can then fall onto the substrate and form a thin film.

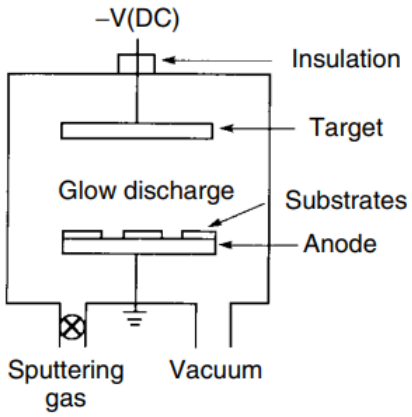

Figure 2.3: *A DC sputtering system imported from [28].*

2.1.4 Atomic Layer Desposition

Atomic Layer Deposition (ALD) grows a thin film of metal oxide using a chemical surface-controlled reaction [28]. The reaction comes in an alternative step fashion. In the first step, reactant gas molecules such as H_2O are chemisorbed by the substrate surface in their first layer. The following layers are physisorbed. Since the bond energies regarding the first layer and higher layers have a significant difference, also different for their desorption time, one can choose a recipe with an appropriate temperature and flush pulse frequency so that only the first layer remains and others are flush away. Next, the gas composed of the target metal element, for example, $HfCl_4$ reacts with

the first layer, producing desired metal oxide HfO_2 and a gas HCl that can be flushed away.

During the whole process, two recipes of the dielectric layer are fabricated, including HfO_2 + AlO_x(aluminum oxide is the lower layer so that hafnium oxide separates it from the aluminum superconductor on their top) and pure HfO_2.

2.1.5 Nanowire Growth Technique

InSb nanowire is one of the most important ingredients in the Kitaev device. It has strong spin-orbital interaction [29] and hence potentially enables p-wave superconductivity. The nanowires in this project are grown by scientists from TU Eindhoven using an innovative approach Metal Organic Vapour Phase Epitaxy (MOVPE) with Selective-area Vapour Liquid Solid (SA-VLS) technique [30].

The most significant advantage of the SA-VLS technique is to enable vertical and stemless nanowire growth directly on InSb(111)B substrate instead of on a foreign stem such as InP and InAs [31]. To achieve this, the catalyst droplets (gold) are restricted in tiny selective openings on the Si_xN_y mask, so that the contact angle of gold always permits nanowire growth. The growth progress of a nanowire is shown in figure 2.4.

In addition, the electron mobility is increased and also the purity of InSb is greatly improved.

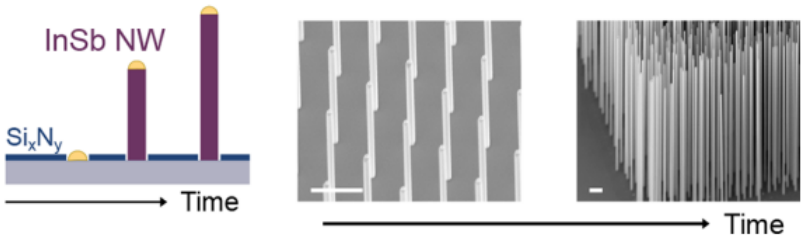

Figure 2.4: *Nanowire growth sketches against time, imported from [30]. The yellowish droplet is the catalyst.*

2.1.6 Smart Wall Technique

The Smart Walls (SW) are solid structures left on the substrate after HSQ negative lithography and development [26], which means that HSQ resist not exposed to electron beam will be removed. In figure 2.5(a), the SW remains open at the superconductor control gate. Evaporated aluminum is shooted to the nanowire through the SW with a cycle composed of 15 degrees and 45 degrees relative to the substrate. The SW is designed to be tall enough so that most of the nanowire lies in the shadow of the wall. The region covered with aluminum is highlighted with orange. This region will extend to a tungsten pad for grounding purposes.

It is also important to mention that before aluminum evaporation, a hydrogen cleaning process is strongly essential [32]. In figure 2.5(c), the device is exposed to a flow of atomic hydrogen radicals, which will react with native oxides indicated by the golden edge of the nanowire cross-section. This cleaning process will surely make the barriers between the superconductor and semiconductor cleaner and greatly benefit the ABS states inside the hybrid.

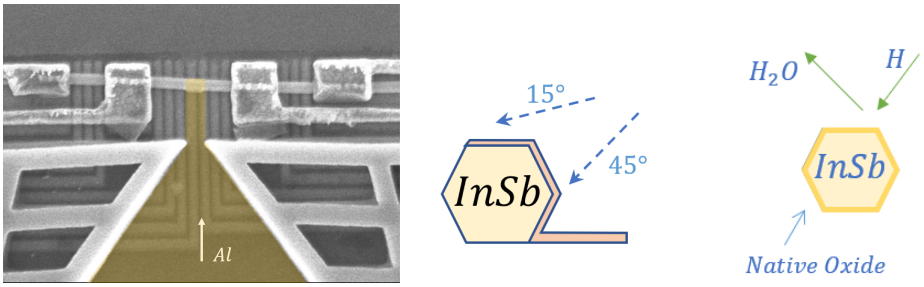

(a) (b) (c)

Figure 2.5: *(a) A planar view of two-site Kitaev device with SW. (b) Cross section at the opening area of SW. Aluminum is coated on the nanowire. (c) Hydrogen cleaning process.*

2.2 Measurement Techniques

2.2.1 PCB Bonding

To operate the nanoscale gates and leads on the device with electronic instruments, every pad assigned to them will be bonded to a pin on the PCB board. Since the pads are microscale, the bonding process happens under an optical microscope. One of the bonded PCB pictures is shown in figure 2.6.

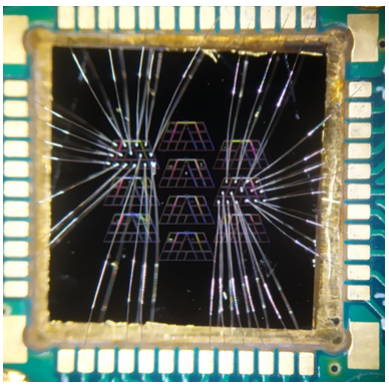

Figure 2.6: *PCB bonding snapshot.*

2.2.2 Dilution Refrigerator at Cryogenic Temperature

After bonding the device, the PCB will be loaded into the dilution refrigerator or fridge and cooled down to approximately 15mK. The full cooling down is divided into several stages. First, the 4.2K ^{4}He bath is a temperature reservoir cooling down the sample to this temperature. The temperature can further cool down to 1.3K by pumping ^{4}He [33].

The cooling down technique at colder temperatures is using phase transitions between helium isotopes ^{3}He and ^{4}He. In figure 2.7, ^{4}He transits into superfluid at the $\lambda-$line, while ^{3}He remains normal fluid. However, at 870mK, the $\lambda-$line is separated into two, which correspond to a ^{3}He-rich phase and ^{4}He-rich phase according to the $x-$axis. If pumping ^{3}He away from ^{4}He-rich phase, ^{3}He will be evaporated from ^{3}He-rich phase and be delivered to the other phase. This will lead to the cooling of the mixture.

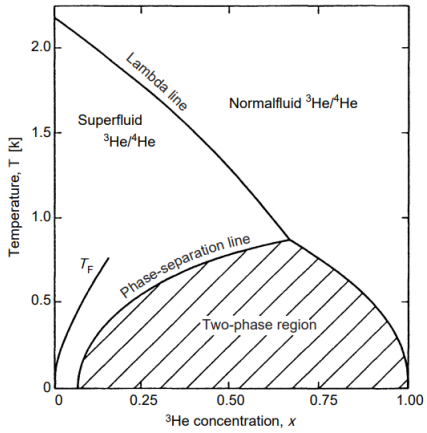

Figure 2.7: *Phase diagram between helium isotopes [33].*

Figure 2.8 shows a helium isotope mixture fridge. To effectively pump ^{3}He from ^{4}-rich phase, the mixture in this phase is connected to a still of 600mK. Since the pressure of ^{3}He vapor is much larger than ^{4}He at this temperature, the pumping is enabled.

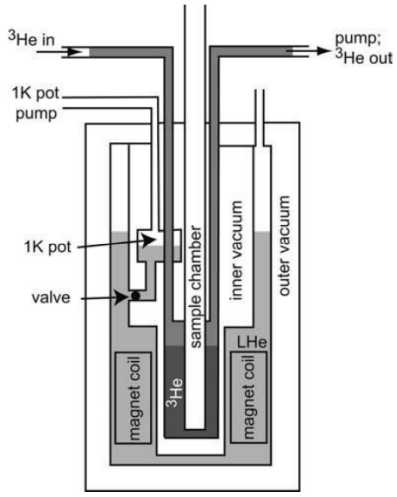

Figure 2.8: *A ^{3}He -^{4}He dilution fridge schematic from [34].*

2.2.3 Instrumentation for Multi-terminal Device

Before diving into the measurement chapters, it is important to mention briefly the peripheral electronics for measurements.

In figure 2.9, two normal contacts and two superconducting contacts are connected to independent sources. The current flow through each source ($I_{0,1,2,3}$) is fed to a corresponding Keithley multimeter ($K_{0,1,2,3}$) isolated by a large impedance. Aside from the DC source, AC amplitude signals can be produced by lockin modules (Lockin_1 and Lockin_2) and they will sit on V_0 and V_3 respectively. Lockin modules on the same side, for example Lockin_1 and Lockin_0, both receive the measured current from K_0, while Lockin_0 is triggered by Lockin_2, meaning that Lockin_1 measures $\frac{dI_0}{dV_0}$ and Lockin_0 measures $\frac{dI_0}{dV_3}$. Lockin_2 and Lockin_3 on the right side measures $\frac{dI_3}{dV_3}$ and $\frac{dI_3}{dV_0}$ respectively.

By choosing two lockin signal frequencies f_1 and f_2 significantly different, the two AC channels are off-resonance. Therefore, they can be measured independently. Ideally, the two superconductor leads can also be assigned to additional lockins.

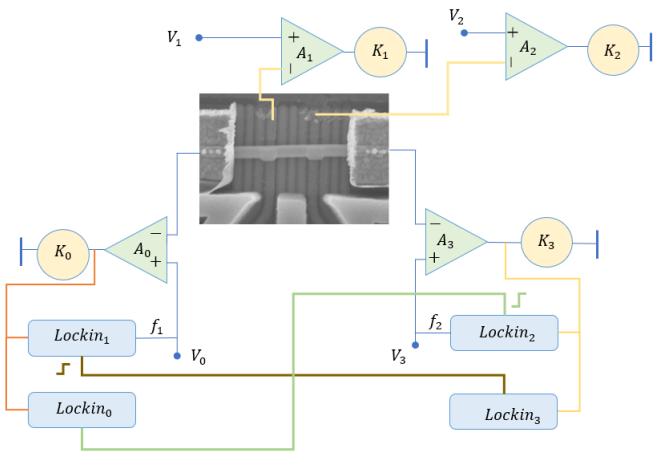

Figure 2.9: *Lockin and DC source setups for local and non-local measurements on a four-terminal Kitaev device.*

Chapter 3

Quantum Transport Processes in a Two-site Poor-Man Majorana Device

The three-site Kitaev device (K-3) is a direct extension of the two-site Poor-Man Majorana (PMM) device which is the minimal implementation of the Kitaev chain proposal [4]. It is worth having a full understanding of the quantum transport processes in the PMM device before stepping into K3. Fortunately, a recent research [15] has already illustrated the feasibility of the PMM proposal proposed by [14] and [13]. Based on previous studies, the main two quantum transport processes are quantitatively studied, including Elastic Co-tunneling(ECT) and Cross Andreev Reflection(CAR). The experiments are conducted in a more compact PMM device, aiming at reproducing PMM signature at the specific sweet points where ECT and CAR are possessing equal strengths.

In addition, this chapter also emphasizes how to establish a systematic as well as efficient procedure to reach the PMM sweet point. In figure 3.1, the main workflow for reaching the sweet point is shown. The first part focuses on characterizing components in the device, including the quantum dots and Andreev Bound States inside the superconducting gap. Various properties of these two components are expected to be observed in order to ensure the components are well-defined. In the second part, the two dots are having interdot couplings. To reach the Majorana Sweet Point, the u and v components of ABS should be finely tuned by the plunger gate. A code is

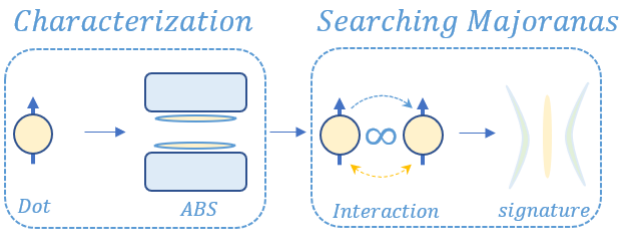

Figure 3.1: *A skeleton of the main workflow for finding Poor-Man Majoranas.*

developed to make the tuning process automatic. Finally, at the sweet point, the signature of the PMM sweet point needs to be checked. An automatic code for this checking is designed for acceleration purposes.

3.1 Device Characterization

The device measured in this study is displayed in figure 3.2(b), along with its previous version on the left. This new design is more geometrically compact since it is intuitive to have more well-delocalized Andreev-bound states (ABS) residing in a shorter hybrid and hence to have the interdot coupling enhanced.

The left and right dots at each side of the hybrid section are respectively defined by three capacitive control gates below the dielectric layer. Taking the left dot as an example, the middle gate $V_{PG,L}$ shifts the dot potential, and the side two $V_{IG,L}$, $V_{OG,L}$ (IG stands for Inner Gates and OG stands for Outer Gates) are controlling the coupling between a dot and hybrid or between a dot and metallic lead. Meanwhile, the middle plunger gate V_{PG} below the hybrid adjusts the energy level and distribution of the sub-gap states in the hybrid. Electrons and holes can be injected into a dot from its corresponding lead with finite voltage biases and can be drained from either the opposite lead or from the grounded aluminum shell. When charged particles are drained, currents can be measured from the leads.

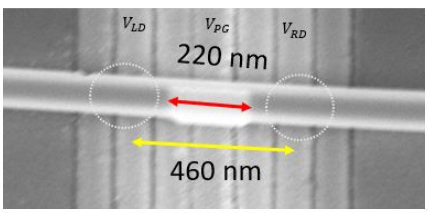

(a)

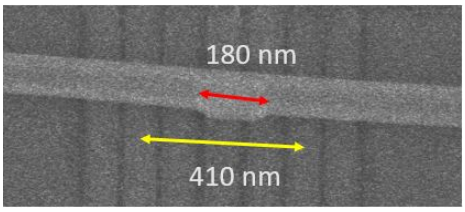

(b)

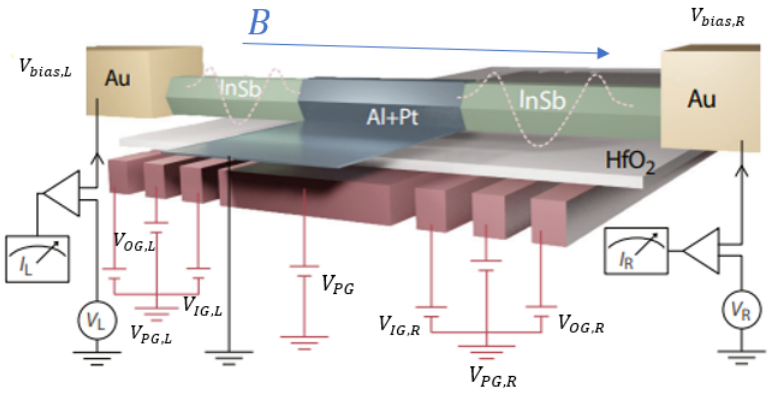

(c)

Figure 3.2: *(a) Old design used in [15] with two dots labeled with grey circles. (b) New design with a shorter range of gates and shorter hybrid section. (c) An overview of the whole system including the peripheral measurement set-ups referred from [15]. An external magnetic field is applied along the nanowire (z-direction), perpendicular to the plane holding the spin-orbit field vector. See Appendix B*

3.1.1 Quantum Dot Characterization

To characterize the dots, the first step is to tune the outer barrier (coupling to lead) and inner barrier (coupling to hybrid) gates so that they can define a quantum dot with clear dot levels. While sweeping the inner gate against the outer gate together, both of them stretch the dot plunger gate by lever arms l_{out} and l_{in}, shown in figure 3.3(b). When the dot potential μ is aligned between the bias source and superconductor drain, a current resonance appears. The resonance is expected to occur in paired parallel lines. The distance between them is proportional to the charging energy if considering electrons on the same orbital.

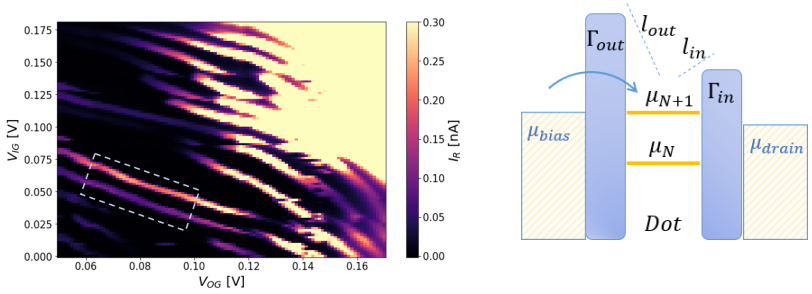

(a) (b)

Figure 3.3: *(a) 2D diagram of $V_{IG,R}$ against $V_{OG,R}$. The left and right middle plunger gates are set off-resonance when plotting each. Bias applied on the right lead is larger than the superconducting gap, so that electrons can be drained to the superconductor. (b) Quantum dot schematic.*

By focusing on the resonances within the dashed line in figure 3.3(a), the parameter space for outer/inner gates can be narrowed down. In the next step, with barriers fixed, the plunger gate of the dot is swept under finite bias larger than the superconducting gap $\Delta \approx 250\mu eV$ on the leads. When dot potential is aligned to the gap edge, electrons can be drained to the superconductor leading to a dot resonance shown in figure 3.4(a). With this method, the coarse dot plunger gate voltage aligning the dot potential to the superconductor gap can be estimated.

The two dot resonances of the same electron orbital are preferred for the experiment. Since the second electron must overcome an additional energy

$E_{add} = 2E_C$ [35] to tunnel into an occupied orbital, they always come in pairs. If the adjacent resonances come from different orbitals, the second electron needs to overcome $2E_C$ plus the orbital energy difference ΔE, which makes the resonance distance farther. The Coulomb diamond in figure 3.4(b) shows that $2E_C = \frac{e^2}{C} \approx 2mV$.

Nevertheless, in many cases, the complicated geometry conditions on the nanowire may give rise to accidental degeneracies on dot, meaning the hybridization of multiple orbitals of electrons. When accidental degeneracies happen on a dot level, a series of dot resonances will show on the 1D resonance map with an equal distance proportional to the charging energy. To verify if a dot level is composed of a single electron orbital, polarization checking with a magnetic field which leads to Zeeman splitting will be effective. The two resonance strips pointed with arrows in figure 3.4(c) show space increasing, meaning a single orbital dot is well defined. A g factor of about 55 can be extracted from the slope.

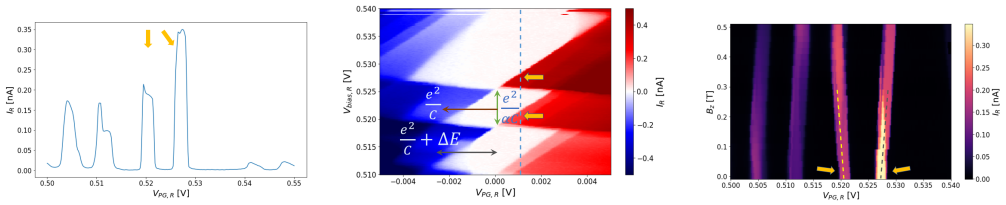

(a) (b) (c)

Figure 3.4: *(a) 1D dot resonance map measured at bias* $1.0mV$ *and zero magnetic field. (b) Coulomb diamonds. 1D resonance map is a diamond slice, shown as the dashed line. The diamond tells the lever arm* $\alpha \approx \frac{1}{3}$ *between the variation of dot potential* $\Delta\mu_R$ *and the variation of the right plunger gate* $\Delta V_{PG,R}$, $-\Delta\mu_R \approx \frac{1}{3}\Delta V_{PG,R}$. *(c) Spin checking for each dot resonance ranging from* $V_{PG,R} = 470mV$ *to* $530mV$ *with an external magnetic field*

3.1.2 Tunnel Spectroscopy of the Hybrid Section

Acting as intermediate states, Andreev Bound States (ABS) are very important for realizing quantum transport between the dots. ABSs are residing in the hybrid section below the superconducting shell. Since the superconducting shell is grounded in this device and there is also a strong coupling Γ

between hybrid and shell, the ground state of ABS tends to be singlet type $|g\rangle = u\,|0\rangle + v\,|\uparrow\downarrow\rangle$ [21].

To detect the energy level of the ABS excitation state, electrons or holes can be injected into the hybrid through the inner barrier, giving rise to the charging and relaxation cycle between the ABS ground state and its excitation state, shown as bright resonance curves in figure 3.5 left panel. Assuming the singlet ground state of an ABS, the electron charges the ground state can either be drained to the opposite lead with strength $|u|^2$ or contribute a hole to the opposite lead with strengths $-|v|^2$. When u competes with v, both of them are functions of the plunger gate V_{PG}, and the non-local conductance on the right panel alternates signs along V_{PG}, shown in figure 3.5.

Furthermore, an ABS with a good non-local response is preferred for the Poor-Man Majorana experiment, since this would exclude the case where ABS is localized on one side of the hybrid. In addition, according to Equ 1.11, an ABS with a lower energy level E_{ABS} is favored for stronger interdot couplings.

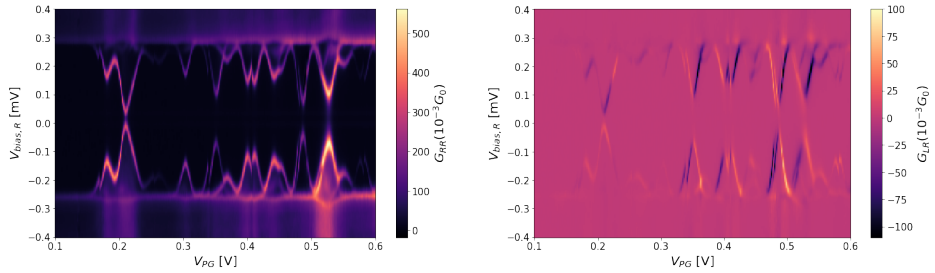

(a) (b)

Figure 3.5: *Spectroscopy with electrons/holes injected from the right lead. Local conductance in the left panel represents dI_R/dV_R measured with the right lockin generator and right receiver. Non-local conductance dI_L/dV_R on the right panel is measured with the left receiver instead.*

3.2 Elastic Co-tunneling and Cross Andreev Reflection in Strong Interacting Regime

3.2.1 CAR and ECT at Zero Field

With the device being characterized, the interaction between the two dots can be studied. The ABS in the hybrid mediates two second-order transport processes CAR and ECT, shown in figure 3.6(a) and 3.6(b) respectively. Especially, since these two processes are second-order virtual processes, they necessarily requires a condition on both lead biases: $|V_{bias,L}|, |V_{bias,R}| < \frac{E_{ABS}}{e}$.

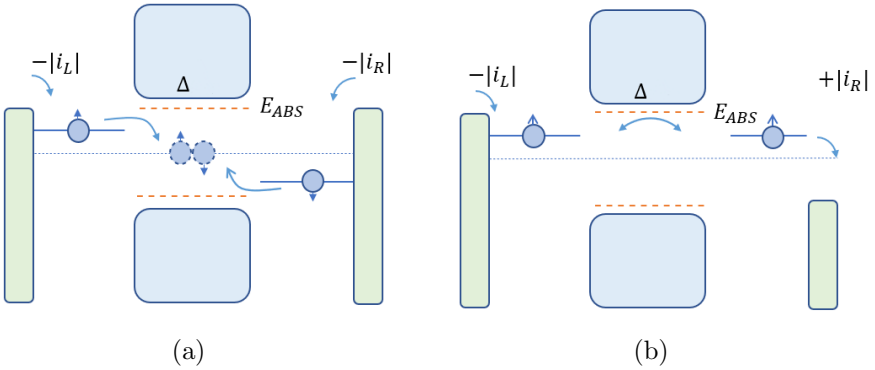

Figure 3.6: *(a) Cross Andreev reflection. (b) Elastic Co-tunneling. The middle blue blocks indicate the gap of the hybrid with sub-gap states.*

ECT and CAR transport processes can be separately studied by applying different voltage bias configurations on the leads. For the case where lead biases are symmetric, $V_{bias,L} = V_{bias,R}$ in figure 3.6(a), only CAR can occur. Dots with potentials opposite to the zero energy enable electrons to condensate into Cooper pairs. However, ECT is forbidden since currents can not flow from one lead to the other. On the other hand, a pair of anti-symmetric lead biases, $V_{bias,L} = -V_{bias,R}$ in figure 3.6(b), enables ECT only. Electrons tunnel from one lead to the other one if the two dot potentials are aligned, leading to a negative sign on the non-local current.

However, if the biases on both leads are neither taking symmetric values nor anti-symmetric values, both ECT and CAR will be allowed. A more detailed

description will be presented in Appendix A. This phenomenon can be used to calibrate the lead biases.

3.2.2 Pauli Spin Blockade at Zero Field

Since each dot level is corresponding to two dot resonances due to spin degeneracy and charging energy, the ECT and CAR transport can indeed happen at all four combinations. To identify the four cases, the charge stability diagram in figure 3.7 is an efficient method.

By labeling dot occupation on each dot level with 1 and 2 or 0 representing no electron occupation, it can be visualized that each case is corresponding to a diagonal or anti-diagonal jumping from one block to the other at one of the four grid points. Specifically, an anti-diagonal jumping labeled with blue arrows indicates normal electron hopping from one site to the other or ECT and the yellow arrows represent Cooper pair condensation/splitting or CAR. Each transition on the charge stability diagram corresponds to charge flowing, which can be measured as a current resonance.

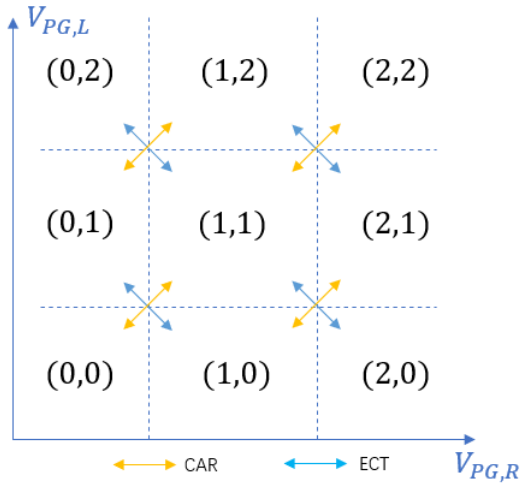

Figure 3.7: *Charge stability diagram*

However, at zero field, the four resonances at all four grid points do not own equal strengths due to Pauli spin blockade effect [36]. Quick explanations

corresponding to spin blockade in CAR transport and its ECT version are sketched in figure 3.8(a) and 3.8(b).

For the first case, due to spin degeneracy at zero field, random spin electrons can tunnel into the dot levels. When spins on two dots are parallel, electrons would neither condense into an anti-parallel spin Cooper pair nor tunnel out of the barriers and hence blockade the transport. This will lead to an absent resonance at $(0,0) \longleftrightarrow (1,1)$ grid point. When including the effect of spin-orbit interaction or SOI, the blockade still cannot be lifted nevertheless [35]. By introducing a gauge transformation [13] on the blockaded eigenstate $|\uparrow\rangle |\uparrow\rangle \rightarrow |\uparrow\rangle |\uparrow\rangle e^{i\phi}$, where L_{SOI} is the hybrid length required for a π precession on the spin and hence $\phi = \pi \frac{L_{SOI}}{L_{hybrid}}$ represents the spin precession angle in the hybrid, the equivalence between the two cases can be understood.

For the other ECT case, the spin conserved transport is blockaded due to Pauli exclusion on the right dot. The blockaded process is mapped to $(0,2) \longleftrightarrow (1,1)$ grid point. By using opposite lead biases, the resonance suffering spin blockade will happen at the remaining two grid points.

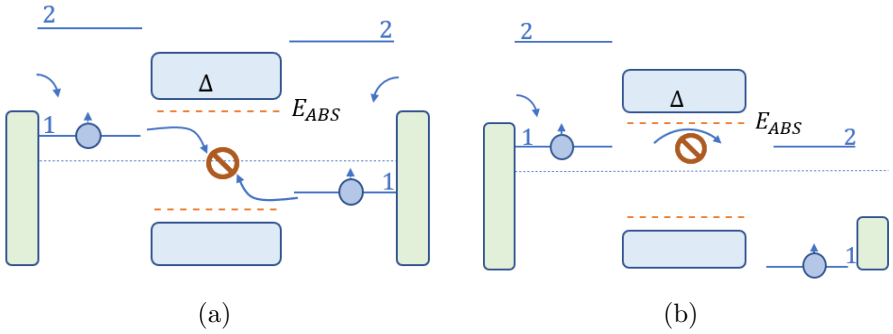

Figure 3.8: *(a),(b) Sketches indicate spin blockade in CAR and ECT configurations.*

The resonance data in figure 3.9 are correlated current synthesized from the right and left currents, which can be expressed as $I_{corr} = \mathrm{sgn}(\mathrm{I_L I_R})\sqrt{\mathrm{I_L I_R}}$ [36]. Ideally, CAR correlation should be in an anti-diagonal linear pattern and ECT correlation is diagonal. However, inelastic components in the transport extend the line segment into a triangle.

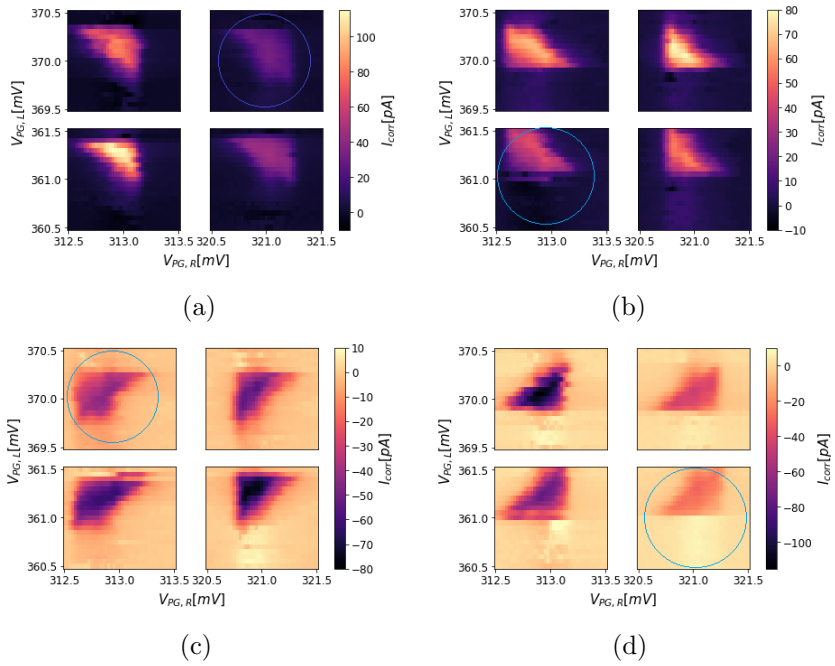

Figure 3.9: *Four resonances in each lead bias configuration. Four kinds of configurations in total. From (a) to (d), biases on leads read as* $(V_+, V_+), (V_-, V_-), (V_+, V_-), (V_-, V_+)$. $V_+ = 80\mu V > 0$ *means lead potential lower than zero energy level and holes are injected.* $V_- = -80\mu V < 0$ *means positive lead potential above zero energy level and electrons are injected. Tiny biases are chosen to make sure electron energy falls below the ABS energy level.*

In each subfigure, the resonance suffering spin blockade is indicated by a circle. The circled current has the minimum among the four, but it is always not completely zero due to several reasons. First, hyperfine interactions from InSb nuclei spins, at the scale of $1\mu eV$ [37, 38], randomly flip the spins of the blockaded electrons according to [39, 40]. An additional reasonable possibility lies in the local Andreev Reflection between dots and superconductors. The blockaded electrons can be drained and the transport cycle revives.

3.2.3 Strong Interacting Regime of Dots

The previous sections are talking about the situation where dots are greatly isolated from the hybrid. Although a coherent sub-gap transport process can be viewed with non-zero lead biases, the dot interactions at zero biases proposed by the PMM proposal could be extremely weak.

A strong coupling between the dots and the hybrid can be realized by lowering the inner barriers between the dots and the superconductor, which is controlled by the inner gates. To illustrate the transition, a series of coulomb diamonds with different inner gate values are plotted in figure 3.10.

Ideally, the electron occupying the dot level below the gap will not tunnel into the superconductor, hence leading to a gap in the middle of Coulomb diamonds. However, with the inner gates increasing from $0.04V$ to $0.06V$, corresponding to lowering the inner barrier, the dot is more proximitized to the superconductor which leads to local Andreev reflection between the dot and superconductor. At this moment, the dot itself starts to behave like an Andreev Bound state, superpositioning the electron component as well as the hole component. The sub-gap eye-shaped ABS levels, shown in figure 3.10(i), directly show the ABS property of the proximitized dot.

According to figure 3.10, the sub-gap feature inside the dot gap could be a good criterion to judge whether a dot is in the Quantum Dot (QD) limit or a proximitized state. Nevertheless, the shape of dot resonance could be a coarse judgment criterion: a sharp dot resonance indicates the QD limit. In the QD limit, the odd parity process ($|01\rangle \leftrightarrow |10\rangle$) and the even parity process ($|00\rangle \leftrightarrow |11\rangle$) are exactly ECT and CAR with couplings t and Δ individually. When the dot is proximitized to the superconductor, these two processes gain extra terms aside from t and Δ due to transport involving hole components. A schematic is shown in figure 3.11. The experiment in this chapter is considered to be conducted at or near the QD limit based on the criterion of the shape of dot resonances.

3.2.4 Poor-Man Majorana Sweet Point at Finite Field

To map a quantum dot chain in reality into a Kitaev chain model, spin degeneracy on each site should be lifted in order to make the electron pairing

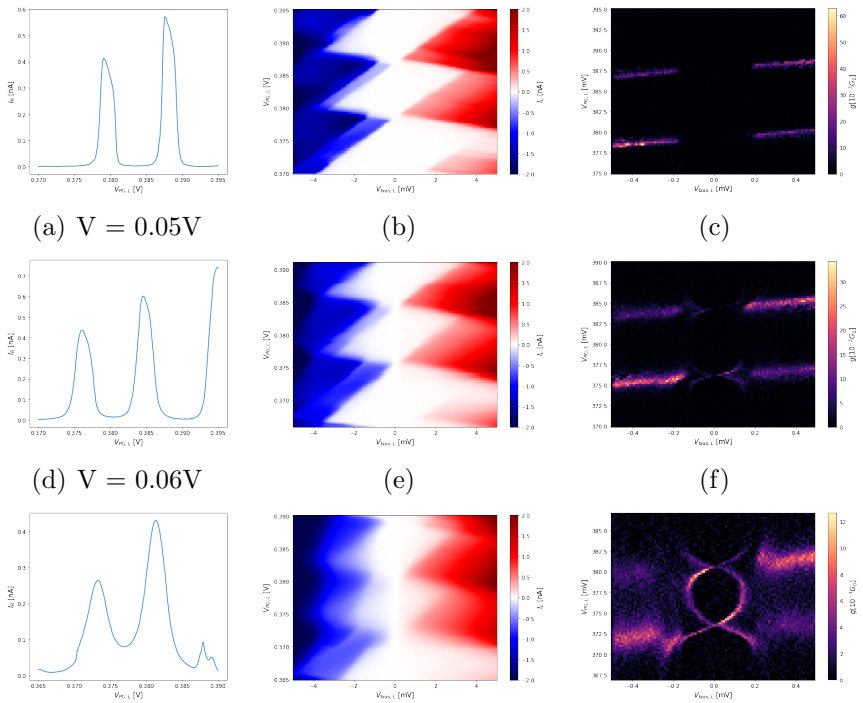

(a) V = 0.05V (b) (c)

(d) V = 0.06V (e) (f)

(g) V = 0.07V (h) (i)

Figure 3.10: *Spectroscopy for left dot. The left inner gate ranges from 0.05V to 0.07V vertically. Corresponding dot resonances and Coulomb diamonds are plotted in the first and second columns. Especially, the third column zooms into the gapped region in the middle of the Coulomb diamond by taking numerical derivatives.*

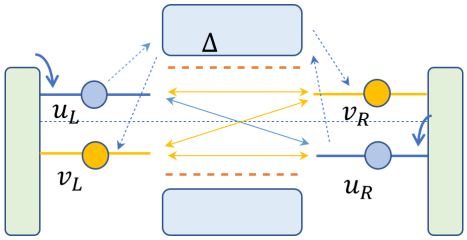

Figure 3.11: *Dots in proximitized regime gain hole components due to local Andreev Reflection, indicated by orange circles. The blue double-arrow shows normal CAR transport and the three other orange double-arrows show extra transport possibilities.*

and hopping processes happen simultaneously among electrons with the fixed spin and hence can be viewed as a spinless system. To engineer this system, the most important ingredient is to have triplet pairing induced by spin-orbit interaction instead of the conventional singlet pairing. When the system is tuned to the sweet point, the interdot couplings of CAR and ECT should satisfy $\Gamma^{CAR}_{\uparrow,\uparrow} = \Gamma^{ECT}_{\uparrow,\uparrow}$. Nevertheless, an equivalent alternative is to achieve unconventional hopping between electrons with anti-parallel spin. With spin-orbit interaction, the amplitude of the opposite-spin hopping $\Gamma^{ECT}_{\uparrow,\downarrow}$ is lifted from zero. The sweet point can thus be expressed as $\Gamma^{ECT}_{\uparrow,\downarrow} = \Gamma^{CAR}_{\uparrow,\downarrow}$.

The thermal noise can be estimated by $3.5k_BT \approx 10.5\mu eV$ with k_B Boltzmann constant and T the electron temperature around $50mK$. To lift the spin degeneracy effectively, Zeeman splitting should be large enough to overcome thermal noise. Given that the g factor extracted from figure 3.4(c) is about 55, a minimal magnetic field $2.2mT$ is required. In fact, the magnetic field applied in the experiments is at least $100mT$, and the energy splitting between two spin states is $2E_z = g\mu_B B \approx 318\mu eV$.

According to the theory chapter, the odd parity state of the interaction Hamiltonian competes for the ground state with the even parity state, forming a boundary of hyperbola shape on the charge diagram $\mu_L - \mu_R$. The transition of parity, corresponding to charge flowing, then leads to a measurable resonance indicating the boundary. The geometry of the resonance can tell if CAR transport dominates ($\Delta > t$) or ECT transport dominates ($\Delta < t$) or at the interesting equal strength point also known as PMM sweet point. For each case, a typical profile is shown in figure 3.12. The three profiles are measured under the same gates and field configuration except for different plunger gate voltages which can tune the relative strengths between CAR and ECT directly [23].

To visualize a transition from ECT to CAR dominance through continuous plunger gate tuning, a series of snapshots of charge diagrams are shown at the bottom row in figure 3.13. From (a) to (e), hyperbolae shrink to a cross and re-split asymmetrically, indicating a transition around $0.45V$.

The scatter-plot in figure 3.13 is composed of correlated currents I_{corr} measured under DC anti-symmetric biases (ECT configuration, blue dots) and DC symmetric biases (CAR configuration, yellow stars) respectively. The

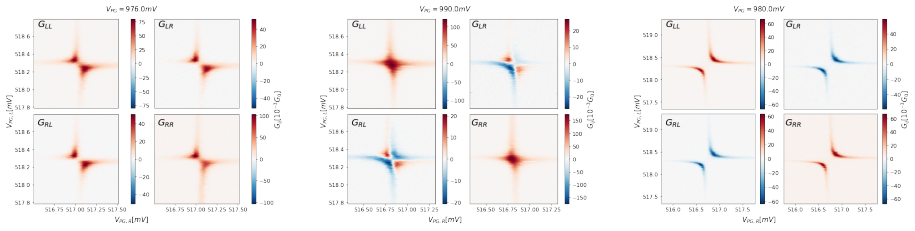

(a) (b) (c)

Figure 3.12: *(a) CAR dominated anti-diagonal hyperbola (b) Cross shape at PMM sweet point. Color-mixed cross at non-local measurement shows competition between the two processes. (c) ECT dominated diagonal hyperbola. External magnetic field* $B = 100mT$*. Local and non-local conductances are measured in unit* $G_0 = \frac{2e^2}{h} \approx 7.75 \times 10^{-5} S$

correlated currents are defined as the maximum square root of the product between left and right measured currents, representing the strengths of CAR and ECT transport individually. Furthermore, the cyan D-line is calculated by $\sqrt{|I_{corr,ECT} - I_{corr,CAR}|} \propto \tilde{D} = \sqrt{8|\Delta^2 - t^2|}$, where $\tilde{D}$ is known to be proportional to the minimum distance between two hyperbola branches on the charge diagram.

Since there is a long interval between charge diagram measurement and scatter-plot measurement, device status changes a little, causing the sweet point indicated by the charge diagram $3 - 5mV$ lower than that indicated by the scatter-plot. Nevertheless, the trends shown by the two approaches match well. The distance between hyperbola branches from (a) to (e) experiences a shrink-expand-shrink process, which agrees with the D-line.

While tuning the plunger gate values, dot levels are affected slightly. To make the whole measurement automatically conducted, resonances should always be tracked by the 2D window. This can be achieved by applying an adaptive code that simply calculates the coordinates of the center of mass of the previous charge diagram and updates the two plunger gates with those new coordinates. However, gate jumps might push the resonance out of the window and lead to loss of tracking, which can be seen from the data point falling out of the trend line in figure 3.13.

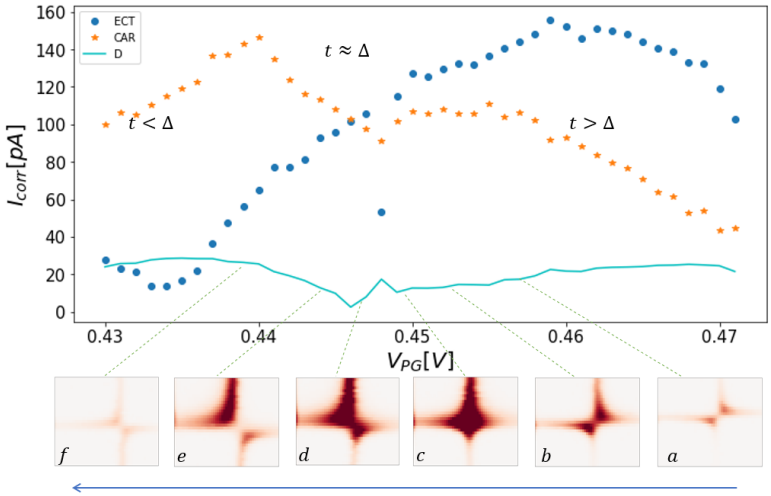

Figure 3.13: *ECT and CAR trend lines against V_{PG} with several snapshots of right local charge diagrams. External field $B = 150mT$. The trend lines are currents measured under CAR and ECT configuration with lead biases $(25\mu V, \pm 25\mu V)$ for each. The snapshots are lockin conductances measured at zero biases.*

3.3 Poor-Man Majorana Spectroscopy

3.3.1 1D Spectroscopy of Zero-bias Peak

So far the Majorana sweet point can be located based on the above procedure. However, to visualize the physics at the sweet point, the center of the cross, where the two dots are aligned to the zero energy level of the leads, should be extracted from the charge diagram. To make this extraction automatic, an intuitive strategy is to track the arms of the hyperbola and calculate the center by using the asymmetry. An example of extracting from an arbitrary hyperbola will be shown in figure 3.14.

In figure 3.14(a), cyan and blue points are the maximum conductance along rows and columns, denoted by the lines with the same colors. The most distant cyan points and blue points labeled by circles respectively give coarse estimation (mean value) on the horizontal and verticle coordinate of the hyperbola center, which is labeled by a purple dot in the middle of two hyperbola arms. The operations in 3.14(b) and 3.14(c) aim at symmetrizing

the cyan and blue point series about the estimated center vertically and horizontally. A point that has no symmetry buddy on the opposite side of the center will be eliminated. After several iterations of these two steps above, a new center is calculated and shown as the orange dot in 3.14(d). This center extraction procedure can deal with charge diagram hyperbola at $\Delta \neq t$ as well as the cross at sweet point $\Delta \approx t$.

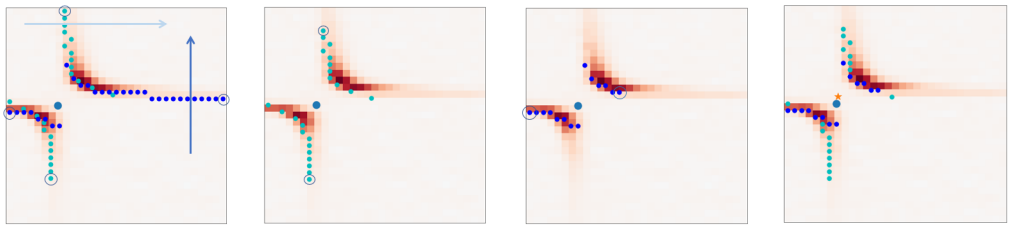

(a) (b) (c) (d)

Figure 3.14: *Center extraction from 2D charge diagram. Background noise below a certain threshold has been removed from the diagram.*

So far it is possible to visualize the theory-predicted zero-bias conductance peak (ZBCP) at the sweet point by setting right and left plunger gate voltages exactly at the cross center and conducting tunnel spectroscopy from lead bias (figure 3.15). Both right and left spectroscopy show ZBCP but with different heights and even much lower than the theory peak $G(T = 0mK) = G_0$, mainly owing to unequal right and left lead-dot couplings $\Gamma_{L,R}^{lead}$ and finite electron temperature($\geq 20mK$, higher than what the dilution fridge measures) among the device. Moreover, a spinless pairing amplitude $\Delta \approx 13\mu eV$ can be extracted from the distance between the two sub-peaks around the ZBCP. Figure 3.15(b) from the right dot shows this standard tri-peak shape, but the left spectroscopy performs pathologically. The reason for left is still unclear.

When changing V_{PG}, the system will be tuned off the sweet point or $t \neq \Delta$, one of the ECT and CAR processes will become the dominant party, and the charge diagram cross at the sweet point degrades into a hyperbola. By placing the dot potentials at the center coordinate of hyperbola, it is expected to see a split ZBCP with a peak interval of $2|\Delta - t|$ at the vicinity of the PMM sweet point, shown in figure 3.16.

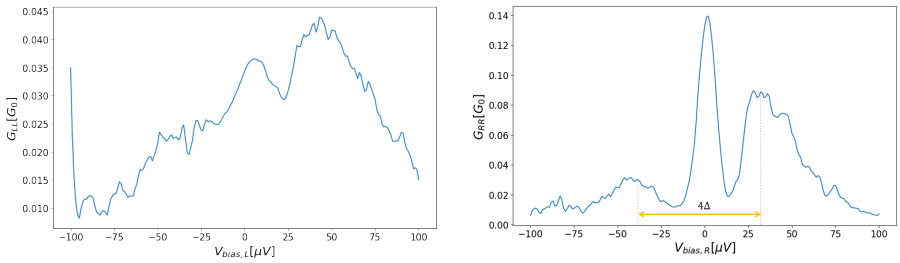

(a) (b)

Figure 3.15: *(a) Local spectroscopy from left. (b) Local spectroscopy from the right. Measured at sweet point where* $V_{PG} = 0.9715V$ *and* $B = 100mT$

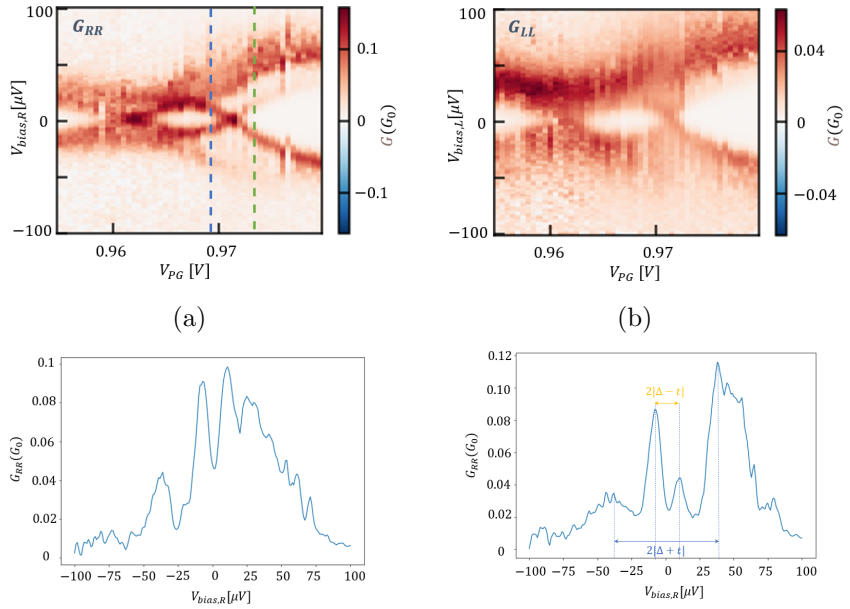

(a) (b)

(c) (d)

Figure 3.16: *(a) Right spectroscopy against* V_{PG}*. (b) Left spectroscopy against* V_{PG}*. (c) Slice took at blue dash line in (a). (d) Slice at green dash line in (a).*

3.3.2 2D Spectroscopy with Perturbations on Dots

When moving one dot potential and fixing the other, the ZBCP at the sweet point $t = \Delta$ will still remain at zero energy. Furthermore, if two dot potentials are moving together away from zero energy, the ZBCP will be lifted from zero energy. To verify these properties of ZBCP, a series of spectroscopies are done, with either left or right dot plunger gate moved, or both of them moved together.

Figure 3.17 plots all four biases against dot potential combinations. And figure 3.18 plots two other cases where two dot plunger gate moves together. Especially, in figure 3.18(a), the parameters ϵ, δ are defined as

$$\begin{cases} \epsilon = \frac{1}{2}(V_{PG,R} - V_{C,R}) + \frac{1}{2}(V_{PG,L} - V_{C,L}) \\ \delta = \frac{1}{2}(V_{PG,R} - V_{C,R}) - \frac{1}{2}(V_{PG,L} - V_{C,L}) \end{cases} \tag{3.1}$$

where $V_{C,L}$ and $V_{C,R}$ are the center coordinates of the hyperbola extracted at the PMM sweet point.

In general, the right spectroscopy in figure 3.17(a) and 3.17(c) matches the theory (shown in Appendix C with details) reasonably [15] but the other two in figure 3.17 involving the left spectroscopy performs not ideally. Furthermore, since Majorana quasiparticles distributed on two dots are chargeless, non-local conductance should remain zero when perturbing the right dot against the right lead bias. However, this conflicts with figure 3.17(a) right panel. A possible reason is that the system is not strictly located on the sweet point due to resolutions and errors on the instruments. The slight deviation off the sweet point might make the two Majorana Bound States not fully separated on the two dots [41].

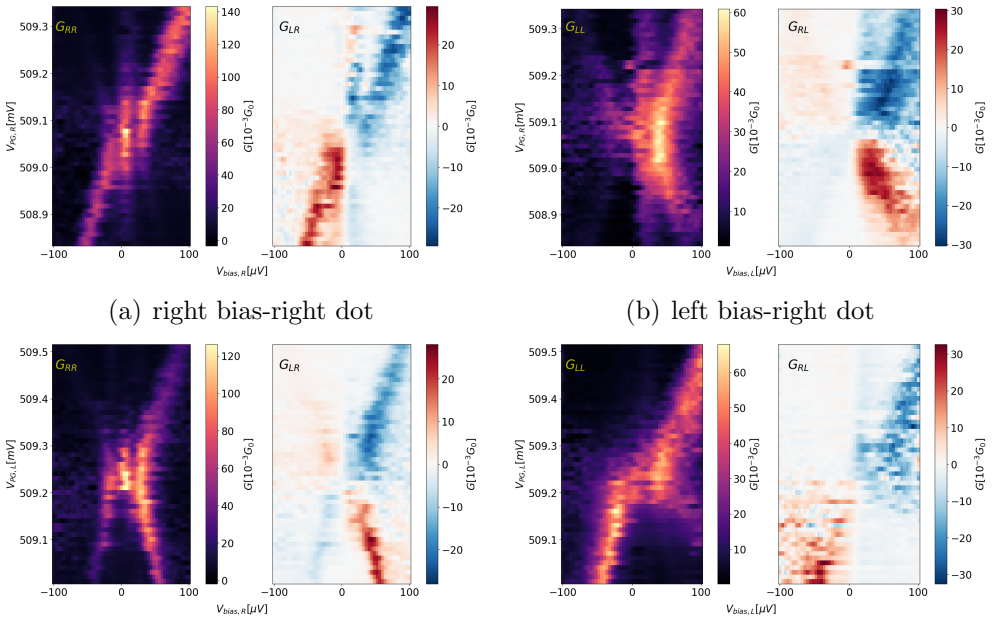

(a) right bias-right dot

(b) left bias-right dot

(c) right bias-left dot

(d) left bias-left dot

Figure 3.17: *Tunnel spectroscopies with only one dot potential perturbated. For each subfigure, the non-local conductance is plotted right to the local conductance. Middle plunger gate* $V_{PG} = 0.969V$*. External field* $B = 100mT$*.*

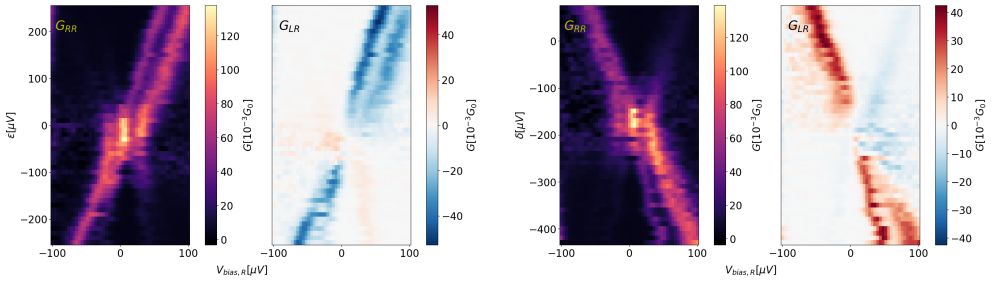

(a) Right spectrum as a function of (ϵ)

(b) Right spectrum as a function of (δ)

Figure 3.18: *Joint dot plunger gate against right lead bias.*

Chapter 4

Quantum Transport on a Three-Site Kitaev Device

In this chapter, electron transport over three sites alternated by two superconductors on a nanowire is studied. So far, the device is not designed with a superconducting loop, so the control on the relative phase between pairing terms Δ_1 and Δ_2 is not discussed.

4.1 Sequential CAR and ECT Processes

The Scanning Electron Microscope (SEM) image of the device is shown in figure 4.1. Dots from left to right are labeled by $i = 1, 2, 3$, and the corresponding control gates for each dot are L_i, M_i, R_i. Using the labels A, B, C, D to the total four leads, the currents, and biases on the superconductor leads are $I_{B,C}$ and $V_{B,C}$. And finally, the two superconductor control gates are S_1, S_2.

Extended from the two-site PMM device, the ideal electron transport from the left to right can be divided into two sequential second-order ECT or CAR processes individually mediated by two ABSs residing in the left and right superconductor. Processes regarding symmetric biases and anti-symmetric biases are shown in figure 4.2.

In figure 4.2(a) and 4.2(b), also called symmetric biases configuration, sequential ECT and sequential CAR is performed by the device. Especially for

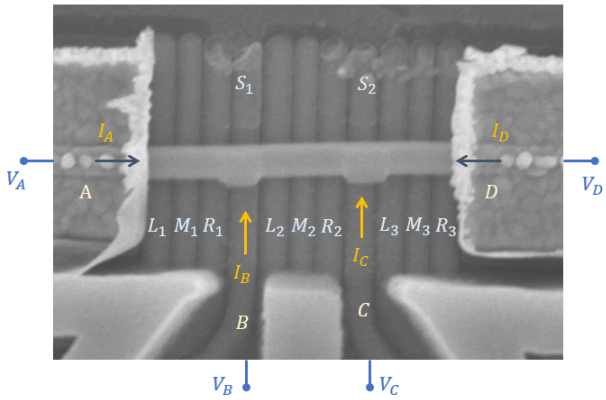

Figure 4.1: *SEM image of three site devices labeled with symbol conventions used in the experiment. Currents along the colored arrows are defined as positive.*

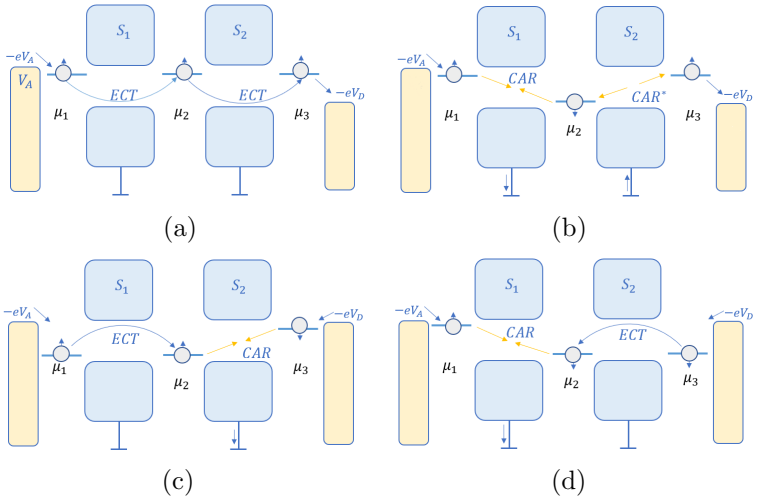

Figure 4.2: *(a),(b) Processes under anti-symmetric biases. (c),(d) Processes under symmetric biases.* $V_{B,C} = 0$ *(grounded)*

sequential CAR, the two processes are composed of one Cooper pair condensing and one Cooper pair splitting (labeled by CAR*), leading to a negative sign of currents measured on the superconductor leads. Since the ECT process preserves charge between the dots, the superconductor lead will detect nothing. For the anti-symmetric configuration, however, CAR and ECT are combined, shown in figure 4.2(d) and 4.2(c). When plotting the current resonance on a cubic 3D charge diagram of μ_1, μ_2 and μ_3, the points where a bright resonance can appear satisfy the following conditions.

$$\begin{cases} \mu_1 = \pm\mu_2 = \mu_3, & V_A = -V_D \\ \mu_1 = \mu_2 = -\mu_3 \text{ or } -\mu_1 = \mu_2 = \mu_3, & V_A = V_D \end{cases} \tag{4.1}$$

If μ_1 is fixed and moving μ_2 and μ_3, ideally two bright points will show on the $\mu_2 - \mu_3$ slice on the cube. The resonance points will converge into one when μ_1 is aligned to zero energy. However, considering the thermal broadening, the resonance will extend into a bright region.

4.2 Device Characterization

Different from the two-site device with each dot being attached to a normal metallic lead, any readout on the middle quantum dot cannot circumvent the adjacent superconducting leads. Therefore, spectroscopy from a superconducting lead needs to be introduced. To verify if the ABS in a hybrid is local or not, spectroscopy is performed between its neighboring superconducting lead and normal lead. Also, spectroscopy from the superconductor can be used to check whether the middle dot is proximitized to the superconductor or not.

4.2.1 Tunnel Spectroscopy

Lockin conductance G_{AA} and G_{DD} are plotted in figure 4.3 when conducting local spectroscopy from the left and right leads. The left superconductor shows a hard gap over a large range of V_{S1} with singlet state ABS in figure 4.3(a). However, the right superconductor shows a weak gap and also ABSs across zero energy. It might be due to a low coupling to the aluminum shell.

To have the non-local signal G_{DB}, for example, the left superconductor lead B is tuned to a "clean" regime at very negative V_{S1}, where sup-gap states

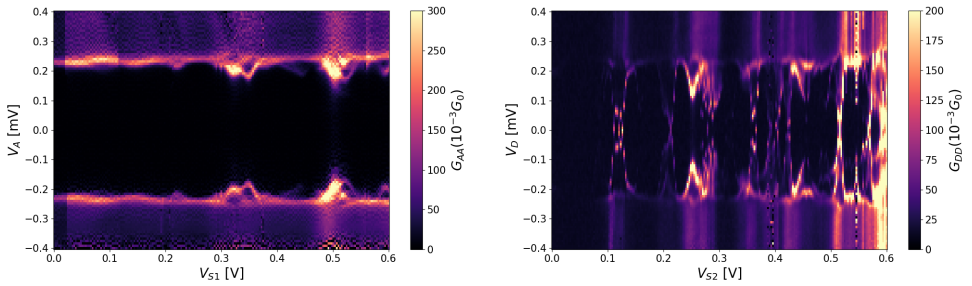

(a) G_{AA} (b) G_{DD}

Figure 4.3: *Local tunneling spectroscopy from left and right leads.*

disappear totally. The DoS of superconductor can be expressed according to [42]

$$\frac{N_S(-eV_B)}{N_N(0)} = \begin{cases} \frac{|eV_B|}{\sqrt{(eV_B)^2-\Delta^2}}, & |eV_B| > \Delta \\ 0, & |eV_B| < \Delta \end{cases} \tag{4.2}$$

Starting from $-eV_B = 2\Delta$ and going downwards, electrons can be injected into the right superconductor from the gap edge DoS of the left superconductor, shown in figure 4.4(a). When $0 < -eV_B < \Delta$, the gap edge providing electrons is already below zero energy. Since no electrons are provided to charge the ABS ground state, an absence of signal occurs in this region.

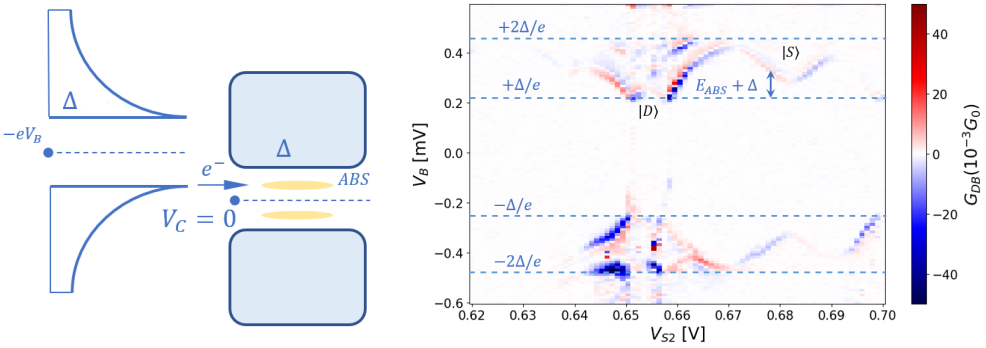

(a) (b)

Figure 4.4: *(a) Superconducting lead working as particle injector. (b) Non-local conductance G_{DB}. $\Delta \approx 230\mu eV$*

The S-S spectroscopy in figure 4.4(b) splits the ABS profiles of the right superconductor into $(\pm\Delta, \pm 2\Delta)$ regions. When the profile touches Δ, an $|S\rangle \leftrightarrow |D\rangle$ ground state transition is triggered. To hunt for singlet ABS, the profile locates higher than Δ is favored. In addition, the resonance current Equ 4.3 experiences a local maximum at $-eV_B = \Delta + E_{ABS}$ due to large DoS at the gap edge and also a large density of ABS state at its ABS level, giving rise to blue negative lockin conductance $\frac{dI_{S\to ABS}}{dV} < 0$ in figure 4.5 aside from the normal reddish positive conductance.

$$I_{S\to ABS} \propto \int_{-\infty}^{+\infty} N_S(E) N_{ABS}(E - eV_B)(f(E) - f(E - eV_B))dE \qquad (4.3)$$

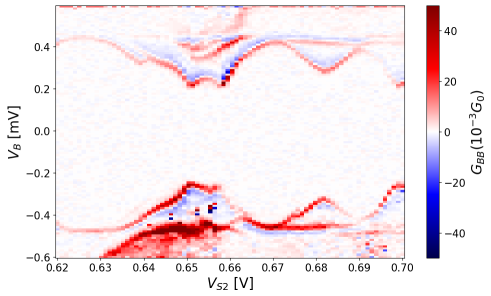

Figure 4.5: *Local conductance G_{BB} probed by superconductor lead.*

This technique can also extend to dot spectroscopy for the middle dot. Spectroscopies are shown in figure 4.6 when the control voltage V_{R2} on the left barrier of the middle dot is switched from $-0.045V$ to $0V$.

4.2.2 Sub-gap Process between two sites

Transport between right and middle dot

When treating superconducting leads as in the previous section, the subgap ECT and CAR processes between two sites can be probed. In figure 4.7, a bias of $-60\mu V$ is applied on the right bias while bias on the left superconducting lead gradually steps from $-310\mu V$ to $+290\mu V$.

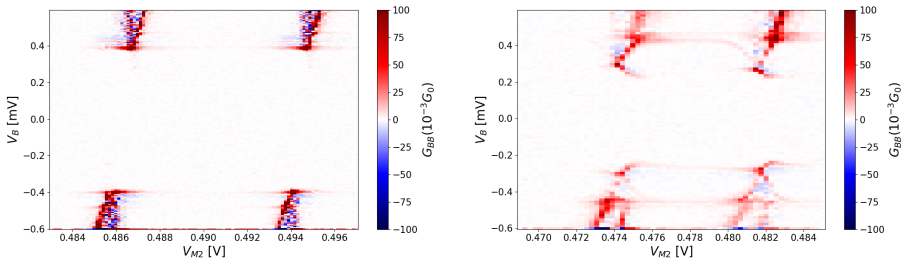

(a) $V_{R2} = -0.045V$ (b) $V_{R2} = 0V$

Figure 4.6: *Middle dot spectroscopy. (a) When the coupling between the middle dot and the right superconductor is low, a clean gap is shown. (b) When switching on the coupling, ABSs are shown.*

When $V_B = -310\mu V$ or figure 4.7(a), given an estimated induced gap of $230\mu eV$, the effective potential on the lead would be $310\mu eV - 230\mu eV \approx 80\mu eV$. The two leads currently have roughly equal biases and hence a CAR signal with tiny ECT residue is observed. When $-eV_B - \Delta < -60\mu eV$, no correlated signal is shown on I_B and I_D. Instead, a little local signal between lead C and D remains, shown in figure 4.7(c). This process will be called shuffling in the following context. The correlated signal will reoccur as an ECT signal when $-eV_B + \Delta < +60\mu eV$. At this moment, the upper gap edge of lead B will drain the co-tunneling electron to the ground, shown in figure 4.7(e) and 4.7(f).

Shuffling process

The remained local current shown in figure 4.7(c) locates at the point where $\mu_2 \approx \mu_3 \approx 0\mu eV$ on the charge diagram. A reasonable explanation is proposed as the *"shuffling process"* shown in figure 4.8. The blue arrow labeled by 1 shows a blue electron that first tunnels into the right dot. Next, it will shuffle to the left dot according to the blue arrow labeled 2. Assuming the left lead cannot drain electrons, the blue electron will wait for the following orange electron to condensate into a Cooper pair. Since the whole process is energy-conserved, the only restriction is $\mu_2 = \mu_3 = 0\mu eV$. The shuffling process can be observed when the electron on one of the dots cannot be drained or is relatively hard to be drained.

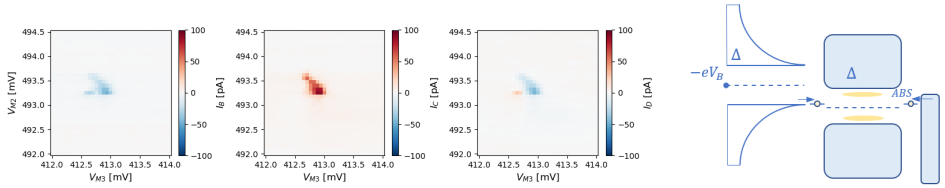

(a) $V_B = -310\mu V$, CAR (b)

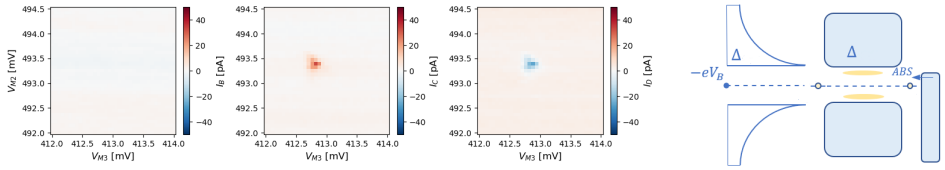

(c) $V_B = -160\mu V$, only shuffling process (d)

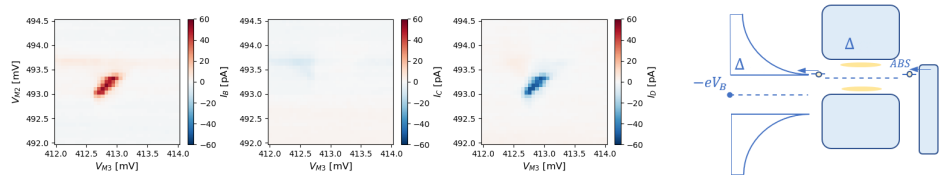

(e) $V_B = +260\mu V$, ECT (f)

Figure 4.7: *(a),(c) and (e) Ramping up the voltage on lead B. The CAR process gradually changes into the ECT process. (b), (d) and (f) Schematics for (a),(c), and (e).*

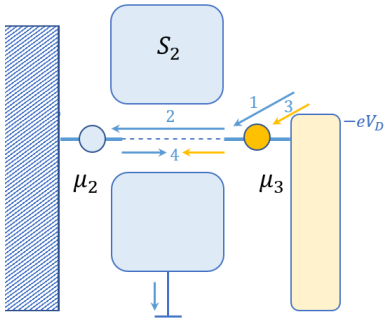

Figure 4.8: *Schematic of shuffling process.*

Transport between left and middle dot

Since the right superconductor gap edge has a weak density of state at negative control voltage, the method using superconductor lead is not able to probe the transport between the left and middle dots. Instead, an alternative solution is used. Keeping $S2$ at high voltage, ABSs populate in the hybrid. By switching on the coupling controlled by the L3 gate, electrons can have accidental tunneling through the superconducting hybrid and hence currents from the right lead can directly feed the middle dot. In figure 4.9, the CAR process is favored and ECT is suppressed.

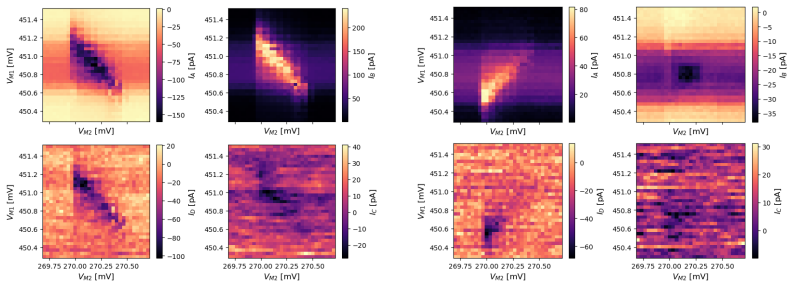

(a) CAR (b) ECT

Figure 4.9: *ECT and CAR at left pair of dots.* $V_A = \mp 75\mu V$ *for (a) and (b) respectively.* $V_D = -75\mu V$ *for both.*

4.3 Sub-gap Process among Three Sites

The final target for this chapter is to show sub-gap transport among three sites. The measurements are conducted under three dot plunger gates V_{M1}, V_{M2}, V_{M3}. To analyze the measured data, slices on the cubic charge diagram with one variable fixed are evaluated.

In figure 4.10, the left and right lead biases, V_A and V_D, are $+110\mu V$ and $-110\mu V$ respectively. After subtracting the current offset on each lead, the currents are plotted in four panels from I_A to I_D. In figure 4.10(a), the left dot potential is out of the bias window and hence off-resonant with $M2$ and $M3$, leading to empty I_A and I_B panels. At this moment, a shuffling process exists between the right normal lead and the right superconducting lead, shown in the circled area. At $V_{M1} = 296.1mV$, the left dot potential

enters the bias window already. The signals circled on panel I_A and I_D in figure 4.10(b) with opposite signs together show a sequential ECT transport. Since ECT transport does not send electrons into the superconducting leads, panels I_B and panel I_C do not show any signals at the same place. On the other hand, the signals labeled with a rectangle show alternated signs from I_A to I_D, which indicates a Cooper pair splitting between the left and middle dots, and a Cooper pair pairing process between the middle and right dots. Additional data measured at other V_{M1} will be shown in Appendix D.

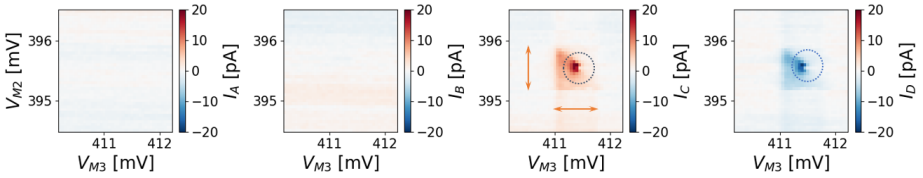

(a) $V_{M1} = 295.7mV$, dot $M1$ off resonance

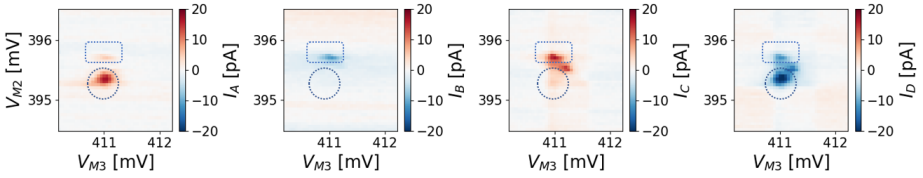

(b) $V_{M1} = 296.1mV$, dot $M1$ on resonance

Figure 4.10: *(a) V_{M1} is not in the lead bias window. The range of the bias window is shown as the orange double-arrows in panel I_C. Current offsets are +3.1pA, +1.3pA, -1.5pA and +1.8pA from left to right. (b) V_{M1} enters the lead bias window and participates in the sequential transport. Current offsets are +6.8pA, -0.7pA, -0.7pA, +0.3pA. Current offsets are extracted automatically from the mode of I values on each plot.*

When the leads are symmetric, for example, $V_A = V_D = -110\mu V$, the sub-gap transport will be a combination of ECT and CAR. In figure 4.11(b), a pair of signals with opposite signs between panel I_C and panel I_D shows CAR between the right and middle dots. Meanwhile, an ECT process is taking place between the middle and left dots.

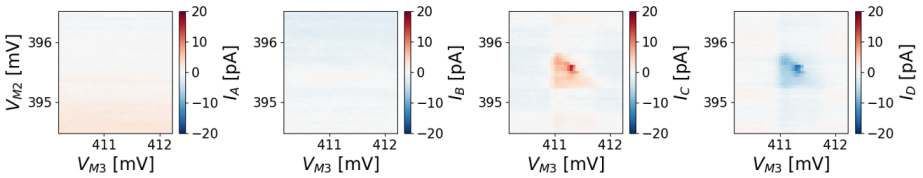

(a) $V_{M1} = 295.7\text{mV}$

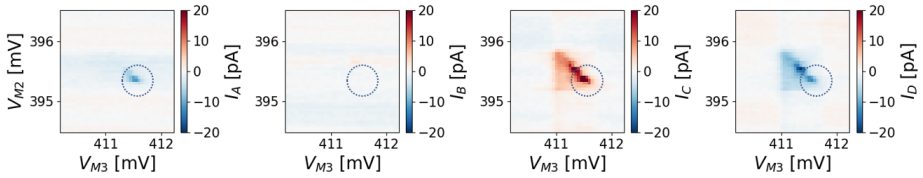

(b) $V_{M1} = 296.1\text{mV}$

Figure 4.11: *Sequential ECT and CAR at symmetric lead biases. Current offsets in (a): +2.9pA, +1.8pA, +0.1pA and +0.7pA. Offsets in (b): +3.3pA, +2.3pA, -2.8pA and -0.4pA*

Conclusion

In the first part of the project, the Poor-Man Majorana signature is reproduced on a two-site chain. A systematic procedure is designed to efficiently tune the device from a free initial state to the final state holding Majoranas. The device characterization includes essential steps to verify if the dot and superconductor components in the device are well-defined. Also, the characterization gives an estimated region potentially holding Majorana Sweet Point among a huge parameter space.

Furthermore, after having all components tuned, the fine-tuning to the sweet point with $\Delta = t$ can be conducted automatically using adaptive code to track the interdot coupling resonance. This automatic tuning procedure illustrates a continuous transition from ECT dominance to CAR dominance interdot coupling. Besides, by extracting the center of the interacting hyperbola, the properties of the Majorana signature can be studied automatically as well, which will accelerate the Poor-Man Majorana searching progress.

The other part of the project focuses on tuning a three-site chain. A modified measurement technique is to use superconducting leads to probe the middle dot. This provides the non-local property of the Andreev Bound States and indicates whether interdot couplings are existing between the adjacent two sites. Moreover, a 3D measurement over the three sites is conducted, indicating that sequential CAR and ECT processes are happening. On the other hand, the nanofabrication routes and parameters applied for all devices involved with the project are approximately the same, indicating that the recipe is rather stable.

Based on the current experiments, further experiments on the three-site chain will focus on the interdot coupling between each pair of dots, especially be-

tween the outmost left and right dots.

Appendix A

Calibration of Lead Biases

The zero energy levels of the right and left lead are always not equal. The tiny offsets f_R and f_L on the leads could be calibrated by the sub-gap process signal. In figure A.1, the CAR and ECT configurations are broken and the unwanted process (orange) mixes into the main process (blue). In figure A.1(a), by lowering the right lead from $V_R \to V_R - \delta/e$ where the orange process disappears, the two biases then will have the same height. And when increasing the right bias voltage by ϵ/e in A.1(b), the two will have opposite heights. The parameters δ and ϵ tell the quantity of $f_R - f_L$ and $f_R + f_L$ respectively.

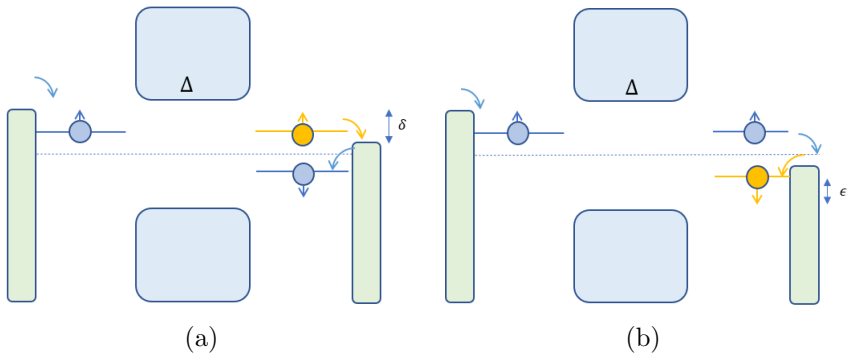

Figure A.1: *(a) CAR configuration with lowered right lead. (b) ECT configuration with higher right lead.*

Real calibration on the device is shown in figure A.2. The biases are $(-100\mu V, -80\mu V)$

for left and right on figure A.2(a), and the heights are calibrated to be equal on figure A.2(b) by lowering right bias by $5\mu V$.

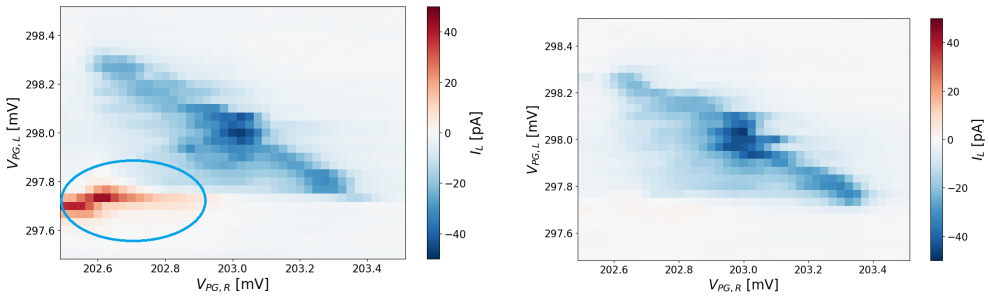

(a) (b)

Figure A.2: *(a) Uncalibrated lead. The red signal circled by the oval is the unwanted ECT process. (b) Lower right lead by* $5uV$*, the ECT component disappears.*

Appendix B

Orientation of Spin-Orbit Field Vector

Because of spin-orbit interaction, electron spins precess around the spin-orbit field vector $\vec{B}_{SOI}$, leading to triplet pairing. When the spin orientation is aligned to $\vec{B}_{SOI}$, the triplet pairing strength is suppressed due to lack of precession [36, 23]. By iterating over all possible B field orientations on the sphere coordinate and measuring the CAR strength between electrons with the same spin meanwhile, the solid angle (ϕ, θ) taking the minimum will indicate $\vec{B}_{SOI}$ [43].

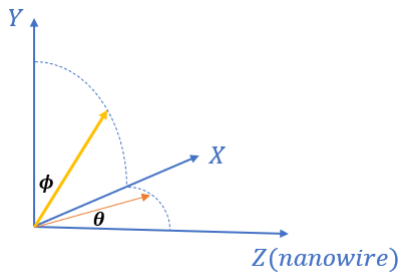

Figure B.1: *Sphere coordinate with Z axis set along the nanowire.*

When performing either azimuthal or polar measurements with a weak field, meaning Zeeman splitting $E_z < \Delta$, the CAR strength can be approximately viewed to be proportional to $\sin^2\phi$ or $\sin^2\theta$ [23, 44]. Correlated CAR

strengths of $\uparrow - \uparrow$ spins against ϕ and θ are plotted in figure B.2. Although only two slices are taken on the sphere, it is enough to estimate that projection of $\vec{B}_{SOI}$ on the X-Y plane heads 95° relative to Y and its projection on the X-Z plane is 85° to Z. The overall orientation is approximately heading X.

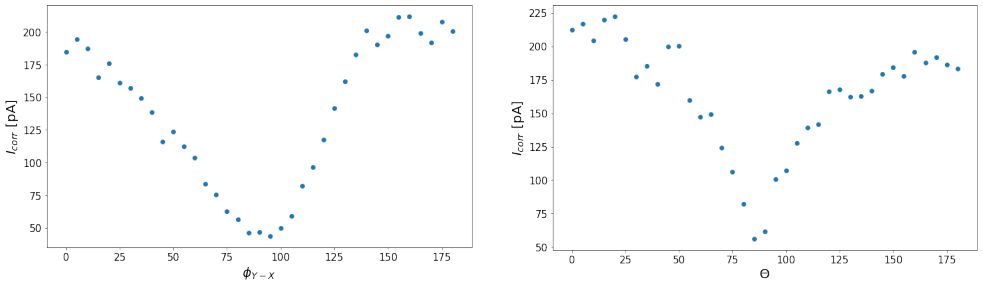

(a) (b)

Figure B.2: *(a) Azimuthal, ϕ_{Y-X} counts from Y axis .(b) Polar*

Appendix C

Theory on Poor-Man Majorana Signature

To probe the density of the state of the Poor-Man Majorana system, spectroscopy will be conducted from the leads coupled to the dots. The S-matrix technique is applied to simulate the lockin conductance of both local spectroscopy and non-local spectroscopy [15]. At zero temperature and in the wide-band limit, the scattering matrix S is given by

$$S(E) = \begin{pmatrix} s_{ee}^{ll} & s_{ee}^{lr} & s_{eh}^{ll} & s_{eh}^{lr} \\ s_{ee}^{rl} & s_{ee}^{rr} & s_{eh}^{rl} & s_{eh}^{rr} \\ s_{he}^{ll} & s_{he}^{lr} & s_{hh}^{ll} & s_{hh}^{lr} \\ s_{he}^{rl} & s_{he}^{rr} & s_{hh}^{rl} & s_{hh}^{rr} \end{pmatrix} = 1 - iW^{\dagger}(E - H + \frac{1}{2}iWW^{\dagger})^{-1}W \quad \text{(C.1)}$$

where W is a diagonal matrix composed of couplings between the dots to the left and right leads Γ_L, Γ_R, $W = diag(\sqrt{\Gamma_L}, \sqrt{\Gamma_R}, -\sqrt{\Gamma_L}, -\sqrt{\Gamma_R})$. H is the Bogoliubov de Gennes formalism of the PMM system, shown in 1.14. Subscript in each element of the scattering matrix s_{ij}^{pq} labels a normal reflection or an Andreev Reflection, where e and h represent electron and hole. Superscript labels the measurement terminal and source terminal with l, r as left and right. In terms of the scattering matrix, the local and non-local conductance is expressed as

$$G_{pq}(E) = \frac{e^2}{h}(\delta_{pq} - |s_{ee}^{pq}(E)|^2 + |s_{he}^{pq}(E)|^2) \quad \text{(C.2)}$$

Simulations conducted by Dr. Chun-Xiao Liu in [15] is shown in figure C.1

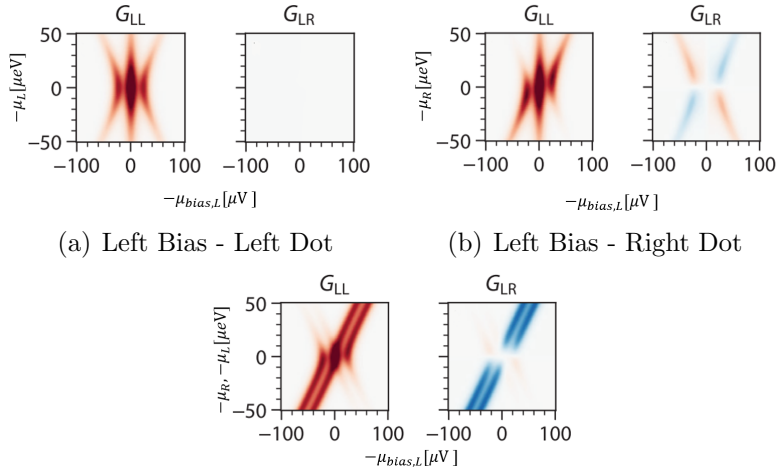

(a) Left Bias - Left Dot

(b) Left Bias - Right Dot

(c) Left Bias - Both Dots

Figure C.1: *Left Spectroscopy. (a), (b) Either moving the potential of the left or right dot. (c) Both dot potentials are moving together.*

Appendix D

Additiona Data for Three-site Device

Figure D.1 provides additional data for the measurement under anti-symmetric bias (figure 4.10). When V_{M1} is ramping across the range of the bias window, the ECT-ECT resonance goes upwards along the diagonal line in panel I_A and I_D. The CAR-CAR resonance does not show a clear trace of going downwards along the anti-diagonal line.

Figure D.2 gives additional data for measurement under symmetric bias (figure 4.11). The ECT(left)-CAR(right) resonance goes along the anti-diagonal line, however, the CAR(left)-ECT(right) resonance is not observed. Moreover, besides the shuffling process on panel I_C and panel I_D, an anti-diagonal but local signal is also existing, labeled by dashed ovals in figure D.2(a). Zoltan *et al* provides a possible explanation in [45] when considering a dot is proximitized to the superconductor or so-called Shiba state [46].

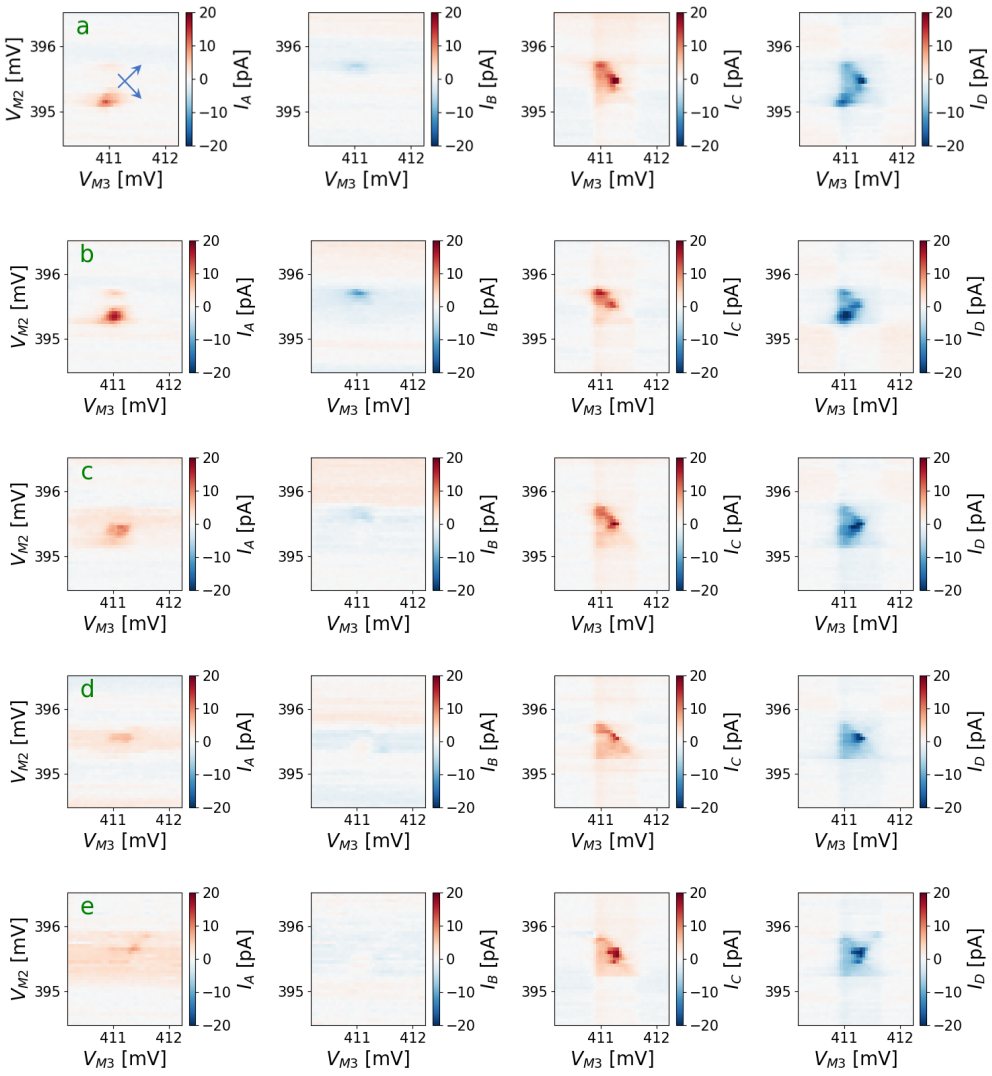

Figure D.1: *Ramping up V_{M1} from 295.95mV to 296.45mV.*

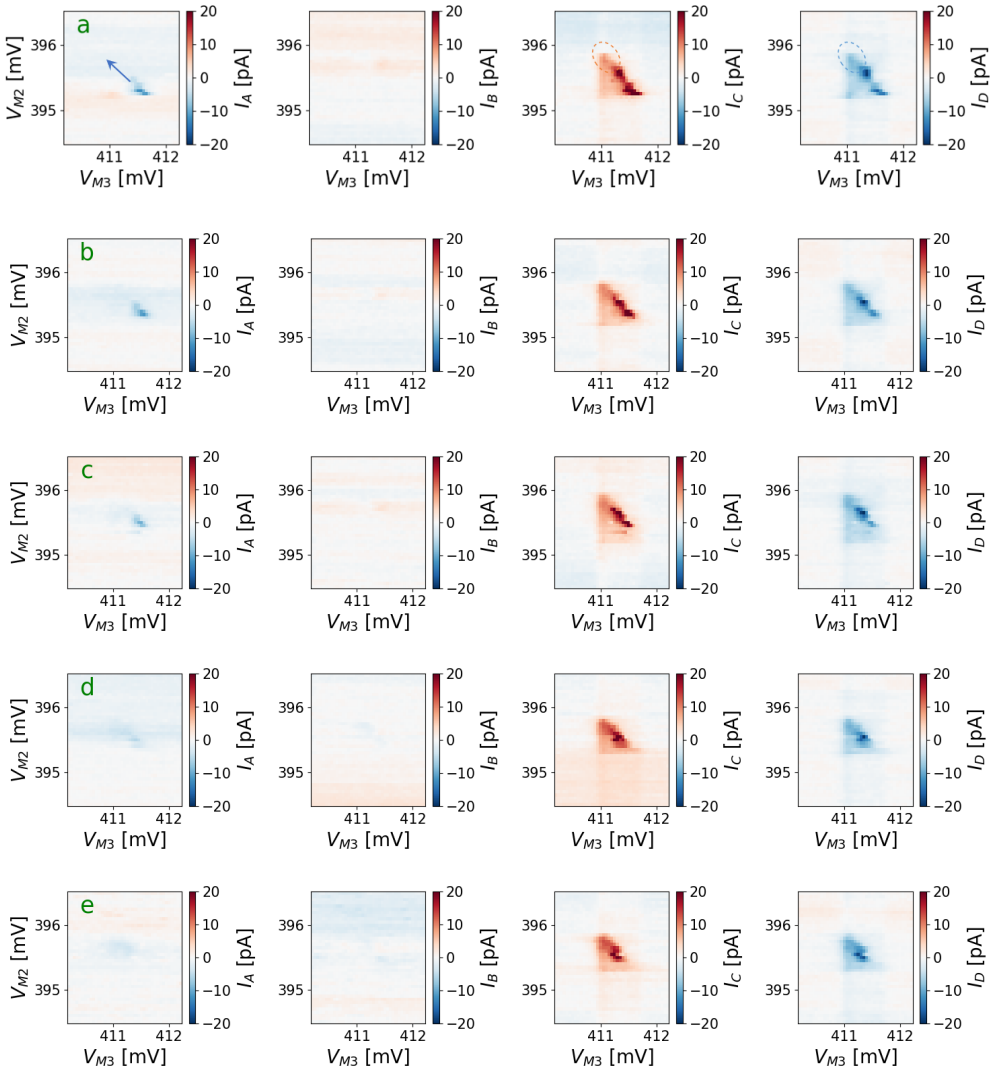

Figure D.2: *Ramping* V_{M1} *up from* $296.0mV$ *to* $296.35mV$.

Acknowledgement

It is my great honor to join the Kitaev team in Kouwenhoven lab and do my thesis project here. As an electrical engineering student without a physics background, people around me provide great help to enable me to explore Majorana physics.

First, I would like to thank my daily supervisors Alberto Bordin and Tom Dvir. To Alberto, I am very grateful that you paid so much effort into training my skills in nanofabrication and measurements. Doing physics experiments on nanoscale chips is always my dream and thank you for making it realized. Besides, I am also affected by your great passion for doing scientific research, which makes me feel motivated during these months. To Tom, I especially admire your genius ideas for designing experiments. Also, your accurate and unique insights into physics deepen my understanding of the systems that I work on.

Next, I want to express thanks to all people who helped me with nanofabrication. Thank you David van Driel, Di Xu, Jan Cornelis Wolff for contributing to the substrate that are very important for the experiments. Besides, thank you Cristina Sfiligoj, Delphine Brousse, Siddharth Singh for the extra cleanroom training at the beginning of the project. Also, I have special thanks to all the Kavli Nanolab staff for supporting the cleanroom.

I would like to thank the group leader Leo Kouwenhoven, who organizes the Kitaev team and supports the great lab. It is a precious opportunity to study here as a master student. Also special thanks to Chun-Xiao Liu, Filip Malinowski, Guanzhong Wang, Nick van Loo and Qingzhen Wang for useful discussions about the Kitaev project. Finally, I will thank all the members of the thesis committee who will spend time reading and evaluating the thesis.

Bibliography

[1] E. Majorana, "Teoria simmetrica dell'elettrone e del positrone," *Il Nuovo Cimento (1924-1942)*, vol. 14, no. 4, pp. 171–184, 1937.

[2] B. M. Leijnse and K. Flensberg, "Introduction to topological superconductivity and majorana fermions," *Semiconductor Science and Technology*, vol. 27, 2012.

[3] A. Stern, "Non-abelian states of matter," *Nature*, vol. 464, no. 7286, pp. 187–193, 2010.

[4] A. Y. Kitaev, "Unpaired majorana fermions in quantum wires," *Physics-Uspekhi*, vol. 44, no. 10S, pp. 131–136, oct 2001.

[5] J. Bardeen, L. N. Cooper, and J. R. Schrieffer, "Theory of superconductivity," *Phys. Rev.*, vol. 108, pp. 1175–1204, Dec 1957.

[6] S. Das Sarma, C. Nayak, and S. Tewari, "Proposal to stabilize and detect half-quantum vortices in strontium ruthenate thin films: Non-abelian braiding statistics of vortices in a px+ ipy superconductor," *Phys. Rev. B*, vol. 73, 11 2005.

[7] L. Fu and C. L. Kane, "Superconducting proximity effect and majorana fermions at the surface of a topological insulator," *Phys. Rev. Lett.*, vol. 100, p. 096407, Mar 2008.

[8] J. D. Sau, R. M. Lutchyn, S. Tewari, and S. Das Sarma, "Generic new platform for topological quantum computation using semiconductor heterostructures," *Phys. Rev. Lett.*, vol. 104, p. 040502, Jan 2010.

[9] R. M. Lutchyn, J. D. Sau, and S. D. Sarma, "Majorana fermions and a topological phase transition in semiconductor-superconductor heterostructures," *Physical Review Letters*, vol. 105, no. 7, aug 2010.

[10] Y. Oreg, G. Refael, and F. von Oppen, "Helical liquids and majorana bound states in quantum wires," *Physical Review Letters*, vol. 105, no. 17, oct 2010.

[11] R. Aguado, "Majorana quasiparticles in condensed matter," *La Rivista del Nuovo Cimento*, vol. 40, no. 11, pp. 523–593, 2017.

[12] D. Pikulin and et al, "A zero-voltage conductance peak from weak antilocalization in a majorana nanowire," *New Journal of Physics*, vol. 14, Dec 2012.

[13] J. Sau and S. Sarma, "Realizing a robust practical majorana chain in a quantum-dot-superconductor linear array," *Nat Commun*, Jul 2012.

[14] M. Leijnse and K. Flensberg, "Parity qubits and poor man's majorana bound states in double quantum dots," *Phys. Rev. B*, vol. 86, p. 134528, Oct 2012.

[15] T. Dvir, G. Wang, N. van Loo, and et al, "Realization of a minimal kitaev chain in coupled quantum dots," June 2022.

[16] L. P. Kouwenhoven, D. G. Austing, and S. Tarucha, "Few-electron quantum dots," *Reports on Progress in Physics*, vol. 64, no. 6, p. 701, jun 2001.

[17] L. Kouwenhoven, C. Marcus, P. McEuen, S. Tarucha, R. Westervelt, and N. Wingreen, "Electron transport in quantum dots," pp. 105–214, 1997.

[18] Y.-J. Doh, J. A. van Dam, A. L. Roest, E. P. A. M. Bakkers, L. P. Kouwenhoven, and S. D. Franceschi, "Tunable supercurrent through semiconductor nanowires," *Science*, vol. 309, no. 5732, pp. 272–275, 2005.

[19] G. E. Blonder, M. Tinkham, and T. M. Klapwijk, "Transition from metallic to tunneling regimes in superconducting microconstrictions: Excess current, charge imbalance, and supercurrent conversion," *Phys. Rev. B*, vol. 25, pp. 4515–4532, Apr 1982.

[20] J. Bauer, A. Oguri, and A. C. Hewson, "Spectral properties of locally correlated electrons in a bardeen-cooper- schrieffer superconductor," *Journal of Physics: Condensed Matter*, vol. 19, no. 48, p. 486211, nov 2007.

[21] E. J. Lee, X. Jiang, M. Houzet, R. Aguado, C. M. Lieber, and S. De Franceschi, "Spin-resolved andreev levels and parity crossings in hybrid superconductor–semiconductor nanostructures," *Nature nanotechnology*, vol. 9, no. 1, pp. 79–84, 2014.

[22] D. Feinberg, "Andreev scattering and cotunneling between two superconductor-normal metal interfaces: the dirty limit," *The European Physical Journal B - Condensed Matter and Complex Systems*, Dec 2003.

[23] C.-X. Liu, G. Wang, T. Dvir, and M. Wimmer, "Tunable superconducting coupling of quantum dots via andreev bound states," May 2022.

[24] E. I. Rashba and Sheka, "Symmetry of energy bands in crystals of wurtzite type ii. symmetry of bands with spin-orbit interaction included," 2015.

[25] I. C. Fulga, A. Haim, A. R. Akhmerov, and Y. Oreg, "Adaptive tuning of majorana fermions in a quantum dot chain," *New journal of physics*, vol. 15, no. 4, p. 045020, 2013.

[26] J. M. de Teresa, *Nanofabrication: Nanolithography techniques and their applications*. IOP Publishing, 2020.

[27] R. C. Jaeger, *Introduction to Microelectronic Fabrication: Volume 5 of Modular Series on Solid State Devices (2nd Edition)*, 2nd ed. Prentice Hall, 2001.

[28] S. Franssila, *Introduction to Microfabrication*, 1st ed. J. Wiley, 2004.

[29] I. van Weperen, B. Tarasinski, D. Eeltink, V. S. Pribiag, S. R. Plissard, E. P. A. M. Bakkers, L. P. Kouwenhoven, and M. Wimmer, "Spin-orbit interaction in insb nanowires," *Phys. Rev. B*, vol. 91, p. 201413, May 2015.

[30] G. Badawy, S. Gazibegovic, F. Borsoi, S. Heedt, C.-A. Wang, S. Koelling, M. A. Verheijen, L. P. Kouwenhoven, and E. P. A. M.

Bakkers, "High mobility stemless insb nanowires," *Nano Letters*, vol. 19, no. 6, pp. 3575–3582, 2019, pMID: 31094527.

[31] M. Borg and L.-E. Wernersson, "Synthesis and properties of antimonide nanowires," *Nanotechnology*, vol. 24, p. 202001, 04 2013.

[32] S. Heedt, M. Quintero-Pérez, F. Borsoi, and et al, "Shadow-wall lithography of ballistic superconductor–semiconductor quantum devices," *Nature Communications*, 2020.

[33] F. Pobell, *Matter and methods at low temperatures*, 3rd ed. Springer, 2007.

[34] T. Heinzel, *Mesoscopic Electronics in Solid State Nanostructures*, 2nd ed. Wiley-VCH, 2007.

[35] Y. V. Nazarov, Y. Nazarov, and Y. M. Blanter, *Quantum transport: introduction to nanoscience*. Cambridge university press, 2009.

[36] G. Wang, T. Dvir, G. P. Mazur, C.-X. Liu, N. van Loo, S. L. Ten Haaf, A. Bordin, S. Gazibegovic, G. Badawy, E. P. Bakkers *et al.*, "Singlet and triplet cooper pair splitting in hybrid superconducting nanowires," *Nature*, pp. 1–6, 2022.

[37] I. A. Merkulov, A. L. Efros, and M. Rosen, "Electron spin relaxation by nuclei in semiconductor quantum dots," *Phys. Rev. B*, vol. 65, p. 205309, Apr 2002.

[38] M. Gueron, "Density of the conduction electrons at the nuclei in indium antimonide," *Phys. Rev.*, vol. 135, pp. A200–A205, Jul 1964.

[39] S. Nadj-Perge, S. M. Frolov, J. W. W. van Tilburg, J. Danon, Y. V. Nazarov, R. Algra, E. P. A. M. Bakkers, and L. P. Kouwenhoven, "Disentangling the effects of spin-orbit and hyperfine interactions on spin blockade," *Phys. Rev. B*, vol. 81, p. 201305, May 2010.

[40] J.-Y. Wang, G.-Y. Huang, S. Huang, J. Xue, D. Pan, J. Zhao, and H. Xu, "Anisotropic pauli spin-blockade effect and spin–orbit interaction field in an inas nanowire double quantum dot," *Nano Letters*, vol. 18, no. 8, pp. 4741–4747, 2018.

[41] A. Tsintzis, R. S. Souto, and M. Leijnse, "Creating and detecting poor man's majorana bound states in interacting quantum dots," *Physical Review B*, vol. 106, no. 20, nov 2022.

[42] M. Tinkham, *Introduction to superconductivity*. Courier Corporation, 2004.

[43] A. Bordin, G. Wang, C.-X. Liu, S. L. D. t. Haaf, G. P. Mazur, N. van Loo, D. Xu, D. van Driel, F. Zatelli, S. Gazibegovic, G. Badawy, E. P. A. M. Bakkers, M. Wimmer, L. P. Kouwenhoven, and T. Dvir, "Controlled crossed andreev reflection and elastic co-tunneling mediated by andreev bound states," 2022.

[44] A. Hofmann, V. F. Maisi, T. Krähenmann, C. Reichl, W. Wegscheider, K. Ensslin, and T. Ihn, "Anisotropy and suppression of spin-orbit interaction in a gaas double quantum dot," *Phys. Rev. Lett.*, vol. 119, p. 176807, Oct 2017.

[45] Z. Scherübl, G. m. H. Fülöp, J. Gramich, A. Pályi, C. Schönenberger, J. Nygård, and S. Csonka, "From cooper pair splitting to nonlocal spectroscopy of a shiba state," *Phys. Rev. Research*, vol. 4, p. 023143, May 2022.

[46] A. V. Balatsky, I. Vekhter, and J.-X. Zhu, "Impurity-induced states in conventional and unconventional superconductors," *Rev. Mod. Phys.*, vol. 78, pp. 373–433, May 2006.